Monthly Notices of the ROYAL ASTRONOMICAL SOCIETY
MNRAS **497,** 3306–3322 (2020) doi:10.1093/mnras/staa2098

The roles of polycyclic aromatic hydrocarbons in dark cloud chemistry: new constraints on sulphur-bearing species

Jixing Ge [1]★ Diego Mardones,[1,2] Natalia Inostroza[3] and Yaping Peng[4]

[1]*Departamento de Astronomía, Universidad de Chile, Camino el Observatorio 1515, Las Condes, Santiago, Chile*
[2]*Centre for Astrochemical Studies, Max-Planck-Institute for Extraterrestrial Physics, Giessenbachstrasse 1, 85748, Garching, Germany*
[3]*Universidad Autónoma de Chile, Facultad de Ingeniería, Núcleo de Astroquímica & Astrofísica, Av. Pedro de Valdivia 425, Providencia, Santiago, Chile*
[4]*College of Science, Yunnan Agricultural University, Kunming, 650201, China*

Accepted 2020 July 10. Received 2020 July 10; in original form 2020 February 11

ABSTRACT

The recent detection of c-C_6H_5CN in the dark cloud TMC-1 provides a new evidence of polycyclic aromatic hydrocarbons (PAHs) in dark clouds. However, knowledge of PAHs in dark cloud chemistry is still very limited. In this study, we investigate the effects of PAHs on the chemistry in dark clouds by coupling published PAH-related chemistry with a gas–grain reaction network. We found that abundances of some ice species, such as OCS, OCN, C_2H_5OH and $HCOOCH_3$, are enhanced by more than two orders of magnitude due to the inclusion of PAHs in the gas–grain chemistry through accretion and subsequent reactions in ice. Especially, combining PAHs with gas–grain chemistry in dark clouds provides an alternative way to reach a good overall agreement of sulphur-bearing species in both the gas and solid phases using the cosmic value of sulphur. With the inclusion of PAHs, CS + O $\longrightarrow$ OCS makes a contribution of ∼5–10 per cent to solid-phase OCS together with CO + S $\longrightarrow$ OCS (∼80−90 per cent), depending on the initial abundances, chemical age and PAH parameters.

Key words: astrochemistry – ISM: abundances – ISM: clouds – dust, extinction.

1 INTRODUCTION

Polycyclic aromatic hydrocarbons (PAHs) contribute about 2–30 per cent of the carbon in the interstellar medium (ISM; e.g. Tielens 2008). These molecules are composed of multiple aromatic rings fused together, forming a planar molecular structure. The aromaticity is due to the resonance of electrons through the rings (delocalized). PAHs have a weak dipole moment but if one of the carbon atoms in the PAH is substituted with a nitrogen atom to form a nitrogenated PAH (PANH), which has a larger dipole moment, then this might be observable in the far-infrared or Millimeter Wave (MW) range. The PAHs are abundant in space and this abundance had been estimated to be $\sim 10^{-7}$ (e.g. Tielens 2008) for various reasons. Allamandola, Tielens & Barker (1985) estimated the interstellar PAH abundance to be $\sim 2 \times 10^{-7}$ with an average number of carbon atoms of $N_C = 20$ and a radius of ∼0.56 Å by fitting the unidentified infrared emission features in the range of 3.3–11.3 μm for the Milky Way. The PAH abundance can also be estimated from the chemical equilibrium. Watson (1976) proposed that the equilibrium concentration of H_2D^+ can be estimated by the DCO^+/HCO^+ density ratio when the reactions of H_3^+ and H_2D^+ with CO are the sources of HCO^+ and DCO^+. By extending this method to consider PAHs, Lepp & Dalgarno (1988) derived an upper limit of PAHs of $\sim 6 \times 10^{-6}$ from the DCO^+/HCO^+ density ratio when the negative charge is mostly in the form of PAH^- with $N_C = 30-50$. For the dark cloud L134N, Lepp & Dalgarno (1988) proposed $X(PAH) < 9.8 \times 10^{-6}$ and $X(PAH^-) < 8.5 \times 10^{-7}$. Also for dark clouds, Wakelam & Herbst (2008) estimated a PAH ($N_C = 30$) abundance of $\sim 3 \times 10^{-7}$ by integrating over a PAH radius range of 3.8–6.0 Å using the dust model $j_M = 1$ from Draine et al. (2007), which was used to reproduce the extinction curves of the Milky Way. Recently, a simple N-bearing PAH c−C_6H_5CN was detected with an abundance of $\sim 5 \times 10^{-10}$ in TMC-1, which could have been formed via the neutral–neutral gas-phase reaction CN + c-C_6H_6 $\longrightarrow$ c-C_6H_5CN + H (McGuire et al. 2018). This hints that PAHs could widely exist in dark clouds from the evidence of observations, if small PAHs (e.g. C_6H_6 and c-C_6H_6CN) are precursors for PAH formation. However, the PAH chemistry in dark clouds is still far from being understood because of the limited observed information of PAHs and limited data from laboratories. For example, we still do not know the explicit composition, sizes and abundances of PAHs, or their chemical effects in the ISM.

However, because of the high estimated abundances of PAHs, previous chemical modelling studies have shown significant effects of abundant PAHs on the gas-phase chemistry in diffuse clouds (e.g. Millar 1992) and dark clouds (e.g. Lepp & Dalgarno 1988; Millar 1992; Wakelam & Herbst 2008), which provides positive effects of PAHs on interstellar chemistry. Especially for dark clouds, a pure gas-phase model, with the inclusion of PAHs made by Wakelam & Herbst (2008), predicted enhanced gas-phase abundances of many molecules (e.g. OCS and CH_3OH with enhancements of up to two orders of magnitude), as a result of reactions with PAHs and/or secondary effects (indirect reactions without PAHs). They showed that PAHs take over the role of electrons to be the main negative charge carriers, and that the typical dark cloud TMC-1 CP prefers PAHs in contrast to L134N. However, their models are limited to the pure gas phase, which is not self-consistent because dust grains play important roles in the depletion of gas-phase species and

★ E-mail: gejixing666@gmail.com

the formation of complex organic molecules (COMs) in ices (e.g. Hasegawa, Herbst & Leung 1992; Garrod, Wakelam & Herbst 2007; Garrod 2008). The disagreements between gas-phase H_2O and SiO noted by Wakelam & Herbst (2008) also need a more self-consistent model with dust grains. In particular, when the big abundance changes of gas-phase species caused by PAHs (Wakelam & Herbst 2008) are transferred to the solid phase through accretion and subsequent surface/mantle reactions, the ice species abundances could be affected.

The aim of the present paper is to study the effects of PAHs on dark cloud chemistry using a gas–grain chemical model. Special attention is paid to the effects of PAHs on ice composition. Because the estimated upper limit of abundances of PAHs is a few 10^{-6} as we have discussed above, the inclusion of PAHs in a gas–grain model might not alter the main ice compositions, which have larger abundances than PAHs. For example, according to the detected ice species in wide physical conditions of massive young stellar objects (MYSOs), low-mass young stellar objects (LYSOs), background (BG) stars and comets (see the lower and upper quartile values of the detection in table 2 of Boogert, Gerakines & Whittet 2015), H_2O has an abundance of $\sim10^{-4}$. Note that CO, CO_2, NH_3, CH_3OH and CH_4 have ice fractions (relative to ice H_2O) of ∼4−43, ∼10−39, ∼4−8, ∼5−23 and ∼3−6, respectively. These ice species will not be altered much by the inclusion of PAHs. However, for some ice species, such as H_2CO, OCN^- and OCS with smaller ice fractions or only upper limits determined (Boogert et al. 2015), the inclusion of PAHs could introduce big changes. In particular, a big enhancement in the gas phase caused by the inclusion of PAHs could introduce significant changes to ice OCS, which is the only detected S-bearing ice species. This could provide new constraints on the S-bearing chemistry in dark clouds, similar to enhancing the S-bearing reaction network (e.g. Vidal et al. 2017; Laas & Caselli 2019).

We have coupled a three-phase gas–grain chemical reaction network with PAH-related chemistry and found that PAHs play important roles in S-bearing species in both the gas phase and ices (solid phase). In Section 2, we describe the three-phase gas–grain dark cloud model with the inclusion of PAHs. Then, in Section 3, we present the effects of PAHs on both gas-phase and solid-phase species using low-metal initial abundances. In Section 4, we show the effects of PAHs with high-metal initial abundances on sulphur-bearing species. In Section 5, we show the impact of PAH size and abundance. We give a summary in Section 6.

2 MODEL

2.1 Chemistry of PAHs

In the ISM, PAHs are likely to be constrained by fitting observations like the PAH with a carbon number of $N_C \sim 20-50$ (e.g. Tielens 2008). According to Wakelam & Herbst (2008), a pure gas-phase model with PAHs of 10 Å produced smaller abundances for many species by only a factor of ∼2 compared with the model with smaller PAHs of 4 Å. Additionally, their models with a PAH size of 4 Å produced the best fit to observed molecular abundances in TMC-1. Thus, we adopt PAHs with a size of 4 Å ($C_{30}H_{14}$) and mass of 374 (amu) in this work. We adopt the integrated fractional abundance, $X(\mathrm{PAH}) = n_{\mathrm{PAH}}/n_{\mathrm{H}} = 3.07 \times 10^{-7}$, of PAHs over a radius range of 3.8–6.0 Å estimated by Wakelam & Herbst (2008). We discuss the impact of the size and abundance of the PAHs in Section 5.

The PAH reaction network was taken from Wakelam & Herbst (2008) and downloaded from the kinetic data base (Wakelam et al. 2012) for astrochemistry.[1] In this network, the electron attachment, recombination of negative PAH ions (PAH^-) with smaller positive ions, and photo-detachment of PAH^- by ultraviolet radiation are treated as in their standard model (Wakelam & Herbst 2008). Positive charged PAHs (PAH^+) were not included because of their lower abundance than that of PAH and PAH^- in clouds with $A_V > 2$ mag (Lepp & Dalgarno 1988; Dartois & D'Hendecourt 1997; Bakes & Tielens 1998), which results in negligible contributions to the chemistry (Wakelam & Herbst 2008).

Although experimental studies have proposed some low-temperature (down to 10 K) formation pathways of PAHs in the cold ISM through some neutral–neutral reactions (e.g. Parker et al. 2012; Thomas et al. 2017), electron attachment of PAH anions (Carelli, Grassi & Gianturco 2013) and some high-temperature (300 K) gas-phase reactions between dehydrogenated PAH anions and neutral species (Demarais et al. 2012), chemical modelling studies of PAHs are very limited due to the incomplete reaction network. Thus, as a first step, we study the effects of PAHs on ice composition to determine/constrain the ice chemistry in dark clouds by directly introducing gas-phase reactions of PAHs with additional accretion and desorption of PAHs into a gas–grain model. It should be kept in mind that PAHs are not chemically active in the sense that there is no chemical reaction changing PAHs except for their ionization degree. Here, we do not consider accretion or desorption from the PAHs but only PAHs on silicate dust grains.

We consider the accretion and desorption of neutral PAHs as for other neutral species in gas–grain models (e.g. Hasegawa et al. 1992; Semenov et al. 2010). The binding energy of PAHs ($C_{30}H_{14}$) is estimated as 20 956 K using the fitted formula as function of N_C and N_H (hydrogen atom number) proposed by Kamp et al. (2017):

$$E_{\mathrm{bind}}(\mathrm{PAH})/k_{\mathrm{B}} = [482 \times (N_{\mathrm{C}} - N_{\mathrm{H}})] + (946 \times N_{\mathrm{H}})\,(\mathrm{K}). \quad (1)$$

This formula is available for PAHs with N_C up to 100. The uncertainties are within ∼10 per cent. Because of the high mass and low thermal velocity of $C_{30}H_{14}$, the accretion time-scale is estimated as $\sim10^6$ yr with a dust-to-gas mass ratio of 0.01, a temperature of 10 K and a gas density of 2×10^4 cm^{-3}. Thus, we expect that the changes to the gas-phase species caused by the inclusion of PAHs (Wakelam & Herbst 2008) will result in changes to species on dust grains before the accretion of PAHs (10^6 yr), because of the interaction between gas and dust grains.

2.2 Model and parameters

To investigate the effects of PAHs in dark clouds, we use the Gas–Grain CHEMistry (GGCHEM) code, which has been used to study various problems in the ISM (Ge, He & Yan 2016a; Ge, He & Li 2016b; Tang et al. 2019; Ge et al. 2020). We updated the two-phase GGCHEM code to a three-phase code following the method proposed by Ruaud, Wakelam & Hersant (2016).

In our model, the original gas–grain rate file was taken from Semenov et al. (2010), which was developed on basis of The Ohio State University (OSU) rate file. It includes gas-phase reactions, surface/mantle reactions, accretion, and thermal and cosmic ray-induced desorption. It should be noted that we do not include reactive desorption (e.g. Garrod et al. 2007) in our models, which could release species from the solid phase to the gas phase. Finally, this gas–grain rate file is coupled with the above PAH chemistry to reach a complete reaction network. In the final rate file, to reach a

[1] http://kida.obs.u-bordeaux1.fr/networks.html

Table 1. Low- and high-metal initial abundances, $n(x)/n_{\rm H}$.

Species	Low-metal[a]	High-metal[b]
H_2	0.5	0.5
He	9.0×10^{-2}	9.0×10^{-2}
C^+	1.2×10^{-4}	1.2×10^{-4}
N	7.6×10^{-5}	7.6×10^{-5}
O	2.56×10^{-4}	2.56×10^{-4}
S^+	8.0×10^{-8}	1.5×10^{-5}
Si^+	8.0×10^{-9}	1.7×10^{-6}
Na^+	2.0×10^{-9}	2.0×10^{-7}
Mg^+	7.0×10^{-9}	2.4×10^{-6}
Fe^+	3.0×10^{-9}	2.0×10^{-7}
P^+	2.0×10^{-10}	1.17×10^{-7}
Cl^+	1.0×10^{-9}	1.8×10^{-7}
PAH	3.07×10^{-7}	3.07×10^{-7}

[a] Data from Semenov et al. (2010) and references therein. [b] Data from the EA2 set of Wakelam & Herbst (2008).

reasonable abundance of HNCO, we added 13 gas-phase reactions of HNCO taken from the University of Manchester Institute of Science and Technology (UMIST) data base for astrochemistry[2] (McElroy et al. 2013), which are missed in the original gas–grain network. We also removed ten reactions related to PAHs because the fluorine-bearing species HC_4N, SiC_2H_3, SiC_4H, H_2C_3 and HC_3 are not in our network. We also removed three duplicate reactions related to $H_2COHOCH_2^+$. All added and removed reactions are listed in Table A1 in Appendix A.

We use a typical dust radius of 0.1 μm. The mass density of the dust grains and the site density are 3.0 g cm^{-3} and 1.5×10^{15} sites cm^{-2}, respectively (Semenov et al. 2010). Following Fayolle et al. (2011), the two outermost monolayers are considered as the surface, as in the three-phase models of Ruaud et al. (2016) with $\beta = 2$. According to Ruaud et al. (2016), the diffusion-to-binding energy ratio in the mantle is fixed as $E^{\rm m}_{\rm diff}(x)/E^{\rm m}_{\rm bind}(x) = 0.8$ and that in the ice surface is set to be the typical value of $E^{\rm s}_{\rm diff}(x)/E^{\rm s}_{\rm bind}(x) = 0.4$. The diffusion energies of the mantle species with $E^{\rm m}_{\rm diff}(x) < E^{\rm m}_{\rm diff}({\rm H_2O})$ are set to be that of H_2O in the mantle, $E^{\rm m}_{\rm diff}({\rm H_2O})$, except for H, H_2, C, N and O with the assumption of water ice. The sticking coefficients of neutral species are unity except for H and H_2, which are calculated by the temperature-dependent formula determined through fitting to experimental data on np-ASW ice (Matar et al. 2010). This formula gives 0.95 and 0.75 for H and H_2 at 10 K, respectively.

We run the dark cloud model with a density of 2×10^4 cm^{-3}, and a gas and dust temperature of 10 K. The extinction and cosmic ray ionization are set to be 10 mag and 1.3×10^{-17} s^{-1}, respectively. We note that there are several sets of initial abundances used for chemical studies (e.g. Wakelam & Herbst 2008; Semenov et al. 2010, and references therein). In order to obtain the big chemical effects generated by the models with different sets of initial abundances, we test two typical sets: low- and high-metal abundances, especially for the sulphur element (8×10^{-8} and 1.5×10^{-5} for low- and high-metal sets, respectively), which could be important for the only S-bearing species OCS detected in ice in dark clouds. The initial abundances we used are listed in Table 1 in which the second column shows the low-metal set from Semenov et al. (2010) that has been widely used for studies of dark cloud chemistry (Ge et al. 2016a, b, 2020; Sipilä et al. 2019). In the third column, we show the high-metal set taken from the EA2 set of Wakelam & Herbst (2008), which is used to reproduce the S-bearing species, as in Vidal et al. (2017) and Laas & Caselli (2019), using enhanced networks.

[2] http://udfa.ajmarkwick.net/

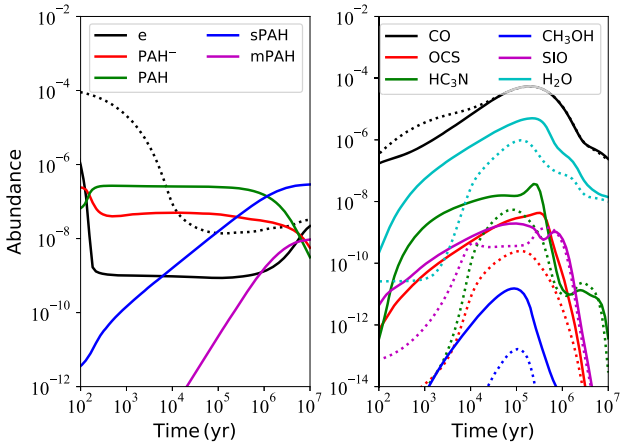

Figure 1. Abundance evolution tracks of selected species from models with (solid) and without (dotted) PAHs. The same species with the same colors. The prefixes 'm' and 's' indicate mantle and surface species, respectively.

Based on this dark cloud model, the effects of PAHs using the low-metal and high-metal sets are presented in Sections 3 and 4, respectively.

3 EFFECTS OF PAHS ON CHEMISTRY USING LOW-METAL ABUNDANCES

3.1 Effects on gas-phase molecular abundances

Our models show similar abundance evolution tracks of PAH, PAH^-, electron (e^-) and other gas-phase molecules as in Wakelam & Herbst (2008) before 10^6 yr. Fig. 1 shows that electrons are replaced by PAH^- to be the main negative charge carrier after 10^2 yr, and some gas-phase abundances of molecules (e.g. OCS and CH_3OH) are enhanced by up to ∼two orders of magnitude before 10^6 yr. We also note that the gas-phase PAH abundance (green solid line) is decreased after 10^6 yr due to the accretion of PAHs. Most PAHs are locked in the dust surface (blue line in the left panel). All of these points mean that the feedback from dust surface reactions is very small due to the cold dust grains (10 K). After $\sim 5 \times 10^6$ yr, because of the accretion of PAHs (green solid line), the electron (black solid line) becomes the main charge carrier again, which results in smaller differences of gas-phase species between models with and without PAHs (see the right panel of Fig. 1).

Generally, our models show similar effects of PAHs on gas-phase species abundances as in Wakelam & Herbst (2008) before 10^6 yr; see more abundance evolution tracks of selected species in Appendix B. By comparing our three-phase gas–grain model with the pure gas-phase model of Wakelam & Herbst (2008), we note that th pure gas-phase model overestimated the abundance of H_2O ($\sim 10^{-6}$) after 10^5 yr, which is similar to that noted by Wakelam & Herbst (2008). This is not consistent with the observed upper limit of H_2O ($\sim 7.7 \times 10^{-8}$) in TMC-1 (Snell et al. 2000). However, when the three-phase model is used, our models with low/high-metal abundances (regardless of the PAHs) produce a comparable H_2O abundance of $\sim 5 \times 10^{-8}$ at a reasonable age of $\sim 2 \times 10^6$ yr (see the cyan lines in Fig. 1) due to the depletion of water in the model with dust grains at a later age.

The above improvement is not a new finding of this work, but only the difference caused by coupling dust grains with gas-phase

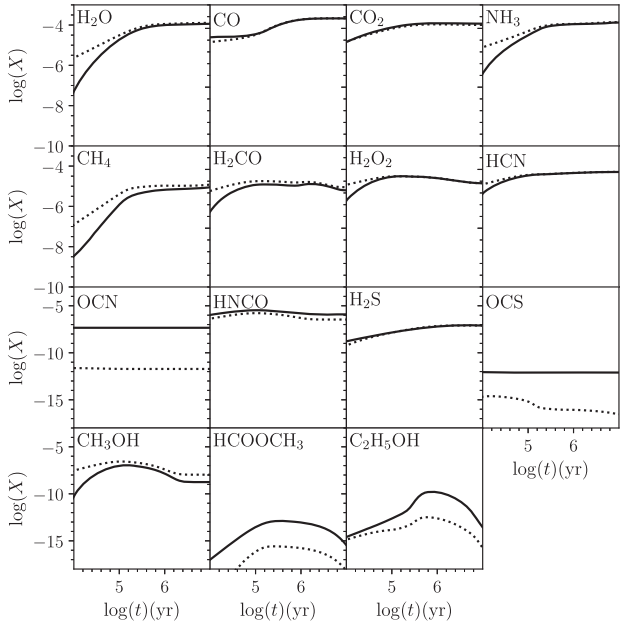

Figure 2. Abundance evolution tracks of selected ice species listed in Table 2 from models without (dotted) and with (solid) PAHs.

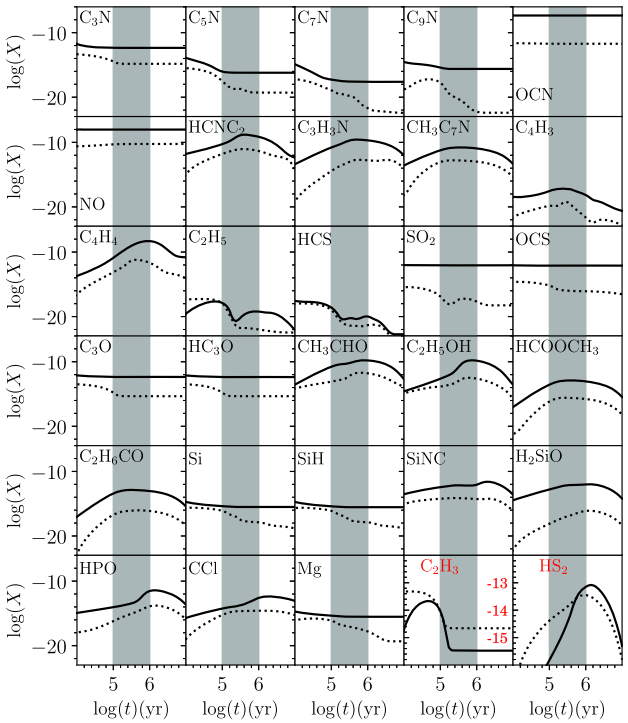

Figure 3. Abundance evolution tracks of selected ice species with enhancements larger than two orders of magnitude caused by PAHs between 10^5 and 10^6 yr (grey region). For C_2H_3 and HS_2 in the last two panels, they have reduced abundances and a zoomed-in *y*-axis (red colour). Black solid and red dashed lines are for models without and with PAHs, respectively.

chemistry. We show that this highlights the fact that combining PAHs with a three-phase model results in a more self-consistent result for some gas-phase species. In the next section, we present the effects of PAHs on the ice component.

3.2 Effects on solid-phase molecular abundances

Fig. 2 shows the abundance evolution tracks of selected ice species that have observed data (Table 2) or large changes due to the inclusion of PAHs. From this figure, we see that, after 10^5 yr, the ice abundance of H_2O is up to $\sim 10^{-4}$, which is comparable to the observed value (1.28×10^{-4}) in Elais 16, a field star close to TMC-1 (Nummelin et al. 2001). We also see that most species (e.g. H_2O, CO, CO_2, NH_3, CH_4, H_2CO, H_2O_2, HCN, HNCO, H_2S and CH_3OH) have small changes after 10^5 yr due to the inclusion of PAHs, except for OCN, OCS, $HCOOCH_3$ and C_2H_5OH, which originally have smaller abundances than PAHs in the model without PAHs.

Table 2. Comparison of ice fractions (relative to ice water, per cent) of selected species between observations and models (with and without PAHs at 10^6 yr). These species are abundant or detected.

Species	$E_{\rm diff}^{\rm s}/E_{\rm bind}^{\rm s} = 0.40$		$E_{\rm diff}^{\rm s}/E_{\rm bind}^{\rm s} = 0.35$		Elias 16[a]	BG stars[b]	MYSOs[b]	LYSOs[b]	L1157[c]
	No PAH	PAH	No PAH	PAH					
H_2O[d]	1.3e−4	1.2e−4	1.1e−4	1.0e−4	1.3e−4	4.0e−5	3.1e−5	3.8e−5	1.0e−4
CO	62	71	51	57	26	20–43	4–15	12–35	–
CO_2	0.94	2.4	20	28	20	18–39	12–25	23–37	–
NH_3	18	17	21	23	<9	<7	∼7	4–8	–
CH_3OH	0.026	0.008	0.035	0.014	<3	6–10	5–23	5–12	0.1–10
H_2O_2	2.1	2.5	1.6	1.8	<5	–	–	–	–
CH_4	7.2	5	9.4	6.8	–	<3	1–3	3–6	–
H_2CO	0.43	0.19	0.72	0.47	–	–	∼2–7	∼6	–
H_2S	0.054	0.057	0.061	0.066	–	–	–	–	
HCN	4.2	4.3	4.5	5.1	–	–	–	–	–
OCN	5.2e−6	0.021	1.7e−6	0.046	–	–	–	–	–
HNCO	0.48	1.3	0.44	1.5	–	–	<0.3–0.7	–	
OCS	1.1e−11	7.9e−8	7.6e−11	8.0e−7	<0.2	<0.22	0.03–0.16	≤1.6	–
$HCOOCH_3$	1.3e−10	7.8e−8	1.5e−10	9.0e−8	–	–	–	–	0.001–0.1
C_2H_5OH	1.8e−7	1.3e−4	2.2e−7	1.5e−4	–	–	–	–	0.0001–0.01
PAH($C_{30}H_{14}$)	–	0.11	–	0.13	–	–	∼8	–	–

[a] Observed data by Nummelin et al. (2001). [b] Collected observed data by Boogert et al. (2015). [c] For C_2H_5OH and $HCOOCH_3$, the fractions are estimated using abundance ratios to CH_3OH of 10^{-2} and 10^{-3}, respectively, in molecular outflow L1157 (Arce et al. 2008), an estimated CH_3OH abundance of 10^{-7}–10^{-5} (e.g. Bachiller & Pérez Gutiérrez 1997; Lefloch et al. 2017) and H_2O abundance of 10^{-4} (Vasta et al. 2012). [d] For H_2O, it is the abundance relative to $n_{\rm H}$.

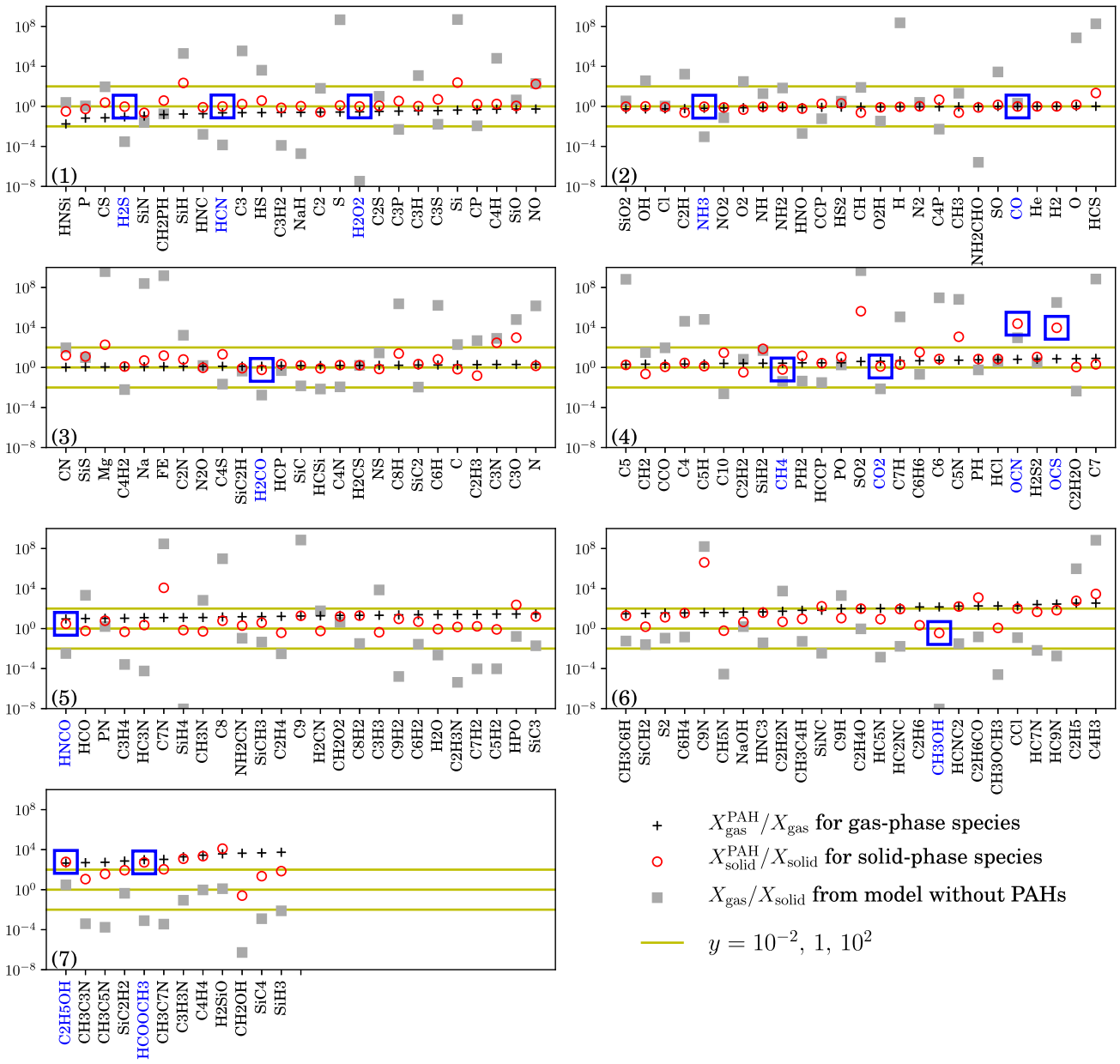

Figure 4. Diagram of abundance changes of 162 neutral species at the chemical age of 10^6 yr. The black crosses show the changes of gas-phase neutral species ($X_{\rm gas}^{\rm PAH}/X_{\rm gas}$) caused by the inclusion of PAHs. The red points indicate the changes of the solid-phase species $X_{\rm solid}^{\rm PAH}/X_{\rm solid}$ corresponding to the gas-phase species. The grey squares show the abundance ratios between gas-phase and solid-phase species in the model without PAHs. Selected ice species are marked with blue boxes and chemical formulas. All species are presented with an increasing order of $X_{\rm gas}^{\rm PAH}/X_{\rm gas}$ from panels 1 to 7.

To explore the general effects of PAHs on ice species, we counted the species with the maximum changes of ice abundances between models without and with PAHs over 10^5-10^6 yr, which covers the typical chemical age ($\sim 3 \times 10^5$ yr) of dark clouds such as TMC-1 and L134N (e.g. Garrod et al. 2007; Majumdar et al. 2017). We show the abundance evolution tracks of selected ice species in Fig. 3 with enhanced abundance $\geq$ two orders of magnitude, $\log(X_{\rm i,ice}^{\rm PAH}/X_{\rm i,ice}) \geq 2$, caused by PAHs. From this figure, we can see that the maximum abundance changes are up to $\sim 10^4$ for some ice species, such as SO_2, C_3H_3N, SiNC and C_4H_4. For most of the selected ice species, the changes are within three orders of magnitude, especially for organic molecules such as C_2H_5OH, CH_3CHO and $HCOOCH_3$. All of these species have abundances smaller than the PAH abundance ($\sim 10^{-7}$), which means that the PAHs only affect ice species with lower abundances than theirs. We also note that there are only a few species that have reduced abundances by more than one order of magnitude, such as C_2H_3 and HS_2, shown in the last two panels of Fig. 3. This means that the inclusion of PAHs causes enhancements for most ice species due to the enhanced gas-phase abundances through accretion and/or subsequent reactions.

Fig. 4 shows the abundance changes of 162 neutral species in both the gas phase (black crosses) and solid phase (red points), which are linked through accretion and desorption, at 10^6 yr. All species are plotted with increasing ratios ($R_{\rm gg}^{\rm PAH} = X_{\rm gas}^{\rm PAH}/X_{\rm gas}$) of gas-phase species between models with and without PAHs (black

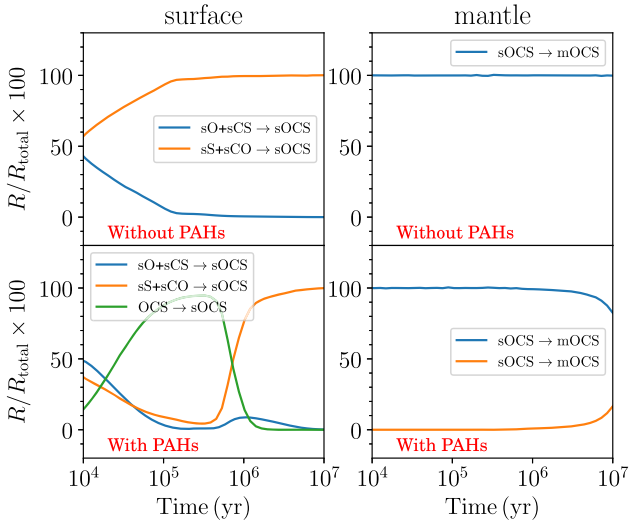

Figure 5. Percentage curve of individual reactions relative to the total production rate for OCS on the dust surface (left panels) and in the mantle (right panels). Upper and lower panels show the results from models without and with PAHs, respectively. Note that the two surface-to-mantle processes in the bottom-right panel are the individual transfer process (blue colour) and the swapping process (yellow colour); see the definitions in Ruaud et al. (2016).

crosses), from panels 1 to 7. Similarly, ratios of solid-phase species $R_{\rm ss}^{\rm PAH} = X_{\rm solid}^{\rm PAH}/X_{\rm solid}$ are shown with red points. A ratio between gas-phase and solid-phase neutral species ($R_{\rm gs} = X_{\rm gas}/X_{\rm solid}$) in the model without PAHs is plotted with a grey square. The selected ice species shown in Table 2 are marked with blue boxes and chemical formulas. From this figure, we see that $R_{\rm ss}^{\rm PAH}$ roughly increases with $R_{\rm gg}^{\rm PAH}$, which hints that enhancements of solid-phase species are mainly due to accretion. We note that the selected ice species in panels 1–4 and 7, such as H_2O_2, H_2, NH_3, CO, CO_2, HCN, CH_4, H_2CO, CO_2 and CH_3OH, have very small changes due to the inclusion of PAHs. This is because the changes of the corresponding gas-phase species are small and the gas-phase abundances are smaller than in the solid phase ($R_{\rm gs} < 1$; grey square), which transfers small effect to the solid phase. However, for ice species such as OCN, OCS and C_2H_5 in panels 5 and 6, they have bigger enhancements. For OCS, the reasons are the enhanced accretion of gas-phase species and the enhanced contribution of reactions in ice. For C_2H_5OH, the enhancement of ice abundance is due to direct accretion of gas-phase corresponding species, which results in similar enhancements in both gas- and solid-phase abundance of C_2H_5OH.

By checking the leading formation reactions of ice species shown in Fig. 3, we can roughly classify these species into six typical groups by the enhancement mechanisms, although the classification is very complicated.

(i) PAHs affect ice abundances through both accretion and reactions in ice. OCS, HCS and C_4H_4 belong to this group. For example, OCS is enhanced by gas-phase reactions $OCS^+ + PAH^- \longrightarrow OCS + PAH$ and $HOCS^+ + PAH^- \longrightarrow OCS + H + PAH$. Then, ice OCS abundance is enhanced by enhanced reactions on the dust surface: $O + CS \longrightarrow OCS$ (∼10 per cent at 10^6 yr) and $CO + S \longrightarrow OCS$ (∼80 per cent at 10^6 yr) together with enhanced accretion (∼10 per cent at 10^6 yr); see Fig. 5. Finally, OCS are quickly transferred from surface to mantle. In Fig. 6, we show abundance evolution tracks of OCS-related species. From this figure, we see that

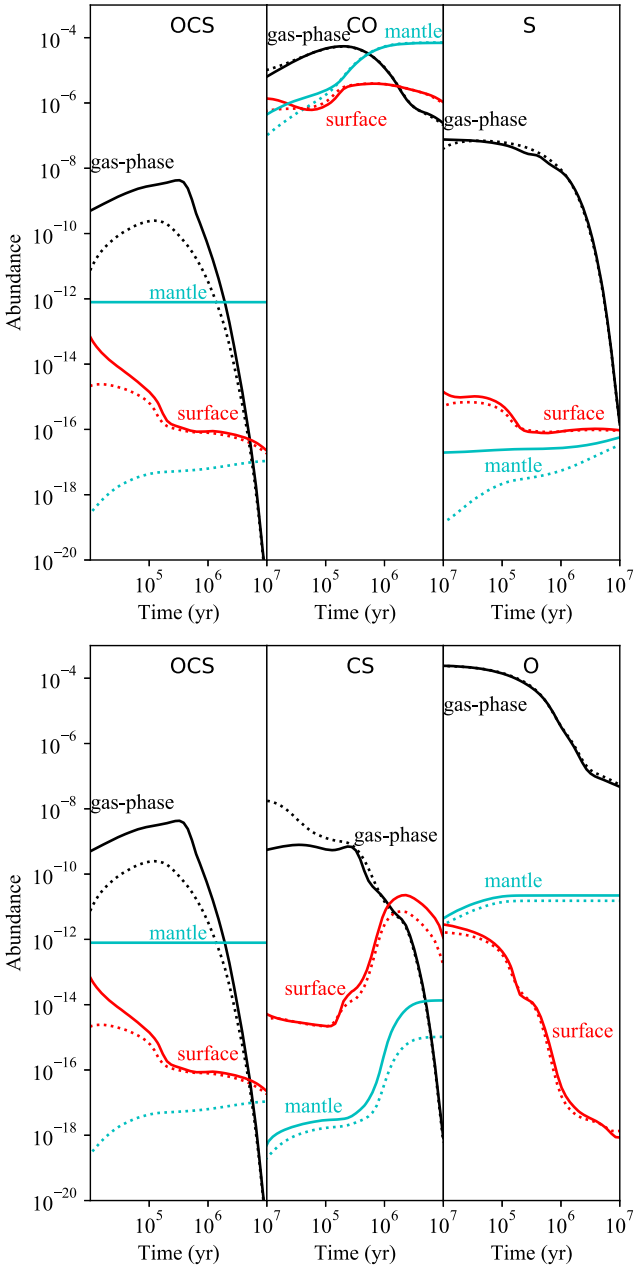

Figure 6. Abundance (with respect to $n_{\rm H}$) evolution tracks of OCS-related species in the gas phase (black lines), dust surface (red lines) and mantle (cyan lines) from models with (solid) and without (dotted) PAHs. Upper and lower panels are for two formation pathways in the solid phase: CO + S ⟶ OCS and CS + O ⟶ OCS, respectively.

CS has enhanced abundance in the solid phase (surface + mantle), which enhances the solid-phase OCS abundance through CS + O. However, only the reaction CO + S in the mantle is enhanced due to the enhanced abundance of S in the mantle. If no PAH is included, only CO + S ⟶ OCS (∼100 per cent at 10^6 yr) is the effective formation pathway in the dust surface; see Fig. 5. Compared with the enhanced network proposed by Laas & Caselli (2019), the surface reaction CS + O ⟶ OCS is new when PAHs are included.

(ii) PAHs affect ice abundances only through accretion and reactions in ice, but there are no PAH-related gas-phase reactions playing an important role in the formation of species in this group. OCN and some carbon chain molecules (e.g. C_nN with $n = 5, 7, 9$) belong to

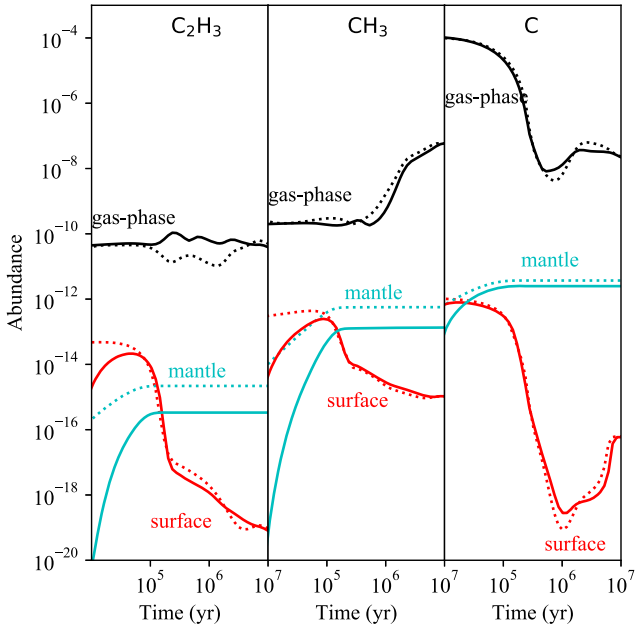

Figure 7. Same as Fig. 6 but for C_2H_3 with one formation pathway in the solid phase: $CH_3 + H \longrightarrow C_2H_3$.

this group. Taking OCN as an example, the abundance of ice OCN is enhanced by enhanced abundances of ice CN and NO, which are due to enhanced abundances of the corresponding species in the gas phase.

(iii) PAHs affect ice abundances through direct accretion. Complex organic molecules (such as C_2H_5OH), Mg, CCl and HPO belong to this group. For example, gas-phase C_2H_5OH is enhanced by $C_2H_5OH_2^+ + PAH^- \longrightarrow C_2H_5OH + H + PAH$ due to the higher abundance of PAH^- than electrons (see Fig. 1), and then transferred to the dust surface and mantle by direct accretions.

(iv) PAHs affect the ice abundance though reactions in the solid phase with a PAH-related gas-phase reaction. SO_2 belongs to this group, which shows that the gas-phase reaction $HSO_2^+ + PAH^- \longrightarrow PAH + SO_2 + H$ becomes the leading formation routine when PAHs are included. However, the enhancement of ice SO_2 is not due to the direct accretion but the enhanced reaction of $O + SO \longrightarrow SO_2$ in both the dust surface and mantle because of the enhancements of ice O and SO.

(v) Although gas-phase C_2H_3 has enhanced abundance due to the inclusion of PAHs (see the black lines in Fig. 7), ice C_2H_3 has reduced solid-phase abundance, as shown in panel 3 of Figs 3 and 4. The reason is that ice C_2H_3 is mainly formed in the mantle through CH_3 + C with CH_3 and C having reduced abundances in the mantle due to the inclusion of PAHs (see cyan lines in Fig. 7). The enhancement of gas-phase C_2H_3 caused by the inclusion of PAHs makes a very small contribution to the solid phase through direct accretion.

(vi) This is a special case with totally new gas-phase reactions and subsequent accretion (e.g. C_2H_5). For C_2H_5, the original reactions between $C_4H_7^+$ (or C_2H_5OH) and e^- are replaced by $C_2H_5^+ + PAH^- \longrightarrow C_2H_5 + PAH$ due to the enhancement of $C_2H_5^+$. Then, subsequent accretion transfers gas-phase C_2H_5 to ice.

We also note that ice C–N–O-bearing species (e.g. C_5N, C_7N, C_9N, OCN and C_3H_3N) have larger changes caused by PAHs than only C–H-bearing species (e.g. C_7H, C_9H, C_9H and C_2H_5); see Figs 2 and 4. This hints that PAHs play important roles in the formation of complex organic molecules. There are many species that have increased or decreased abundances, but we do not discuss these further as there is no observed information to constrain them.

In general, the inclusion of PAHs introduces big changes to solid-phase species due to direct accretion when the original network without PAHs has big abundance ratios between gas-phase species and corresponding solid-phase species (e.g. OCS and C_2H_5OH). Additional reactions in ice make contributions to some species (e.g. OCS, SO_2 and C_2H_3).

3.3 Comparison with observations

3.3.1 Ice compositions

For the ice abundances in dark clouds, we usually compare models with the observed values in Elias 16, which is a field star close to the dark cloud TMC-1. For most of the observed ice fractions (in per cent, relative to ice H_2O), our model with PAHs produces comparable values; see Table 2, where we show two models with different $E_{diff}/E_{bind} = 0.4$ and 0.35 to show the effects mainly on CO_2. The two models show that the observed ice fraction of CO_2 can be reproduced by changing the E_{diff}/E_{bind} within 0.35 and 0.4. For the main ice component with a fraction larger than 1.0 (e.g. H_2O, CO, CO_2, NH_3, CH_4, HCN, and H_2O_2), the effects of PAHs are small because the PAH has a smaller abundance of $\sim 10^{-7}$ in comparison with them (with H_2O abundance of 10^{-4}). For OCS, our models produce an enhanced ice fraction ($\sim 10^{-7}$) by ~four orders of magnitude. Similarly, OCN, C_2H_5OH and $HCOOCH_3$ have enhanced abundances by ~three orders of magnitude due to the inclusion of PAHs.

For ice PAHs, our models predict ~0.1 ice fraction, which is roughly comparable to the summarized value of ~8 for MYSOs by Boogert et al. (2015). If we simply assume that elementary carbons are mainly locked in CO and CO_2 in ice with a total ice fraction of $C_{tot} = 70-80$ (see Table 2), the carbon percentage of PAH can be estimated as $3.7-4.3 = 100 \times (0.1 \times N_C/C_{tot})$, where $N_C = 30$ for $C_{30}H_{14}$. This value is comparable with the value of ~2–30 from observations (e.g. Tielens 2008; Herbst & van Dishoeck 2009).

For ice complex organic molecules (COMs) $HCOOCH_3$ and C_2H_5OH, our models also predict enhanced ice fractions. Although cold dense clouds have no such observed data to compare with our results, we can roughly compare our modelled results with complex molecules in the L1157 outflow in which the observed gas-phase COM abundance enhancements are due to the subsequent sputtering of the dust ice mantle caused by the outflow shock (Arce et al. 2008). Arce et al. (2008) found observed $HCOOCH_3$ and C_2H_5OH abundance ratios with respect to CH_3OH to be 0.01 and 0.001, respectively, in the blue lobe of the L1157 outflow (B1 lobe). According to Vasta et al. (2012), the water abundances are about 10^{-6} and 10^{-4} for low- and high-velocity shock regions in L1157, respectively. In the case that high-velocity shock sputters all the dust mantles, the water abundance of about 10^{-4} is comparable with our models. Using a reported CH_3OH abundance of about $10^{-7}-10^{-5}$ (e.g. Bachiller & Pérez Gutiérrez 1997; Lefloch et al. 2017), the ice fraction of CH_3OH is about $0.1-10$ ($10^{-7}/10^{-4} \times 100$ to $10^{-5}/10^{-4} \times 100$). Considering that the observed $HCOOCH_3$ and C_2H_5OH abundance ratios with respect to CH_3OH are about 0.01 and 0.001, respectively, the ice fractions of $HCOOCH_3$ and C_2H_5OH are estimated as about $0.001-0.1$ and $0.0001-0.01$ accordingly. The value of C_2H_5OH is comparable with our modelled fractions of C_2H_5OH ($\sim 10^{-4}$) when PAHs are included (see Table 2). This hints that inclusion of PAHs may have the potential to account for the formation of COMs in ice in the cold dark cloud stage. However,

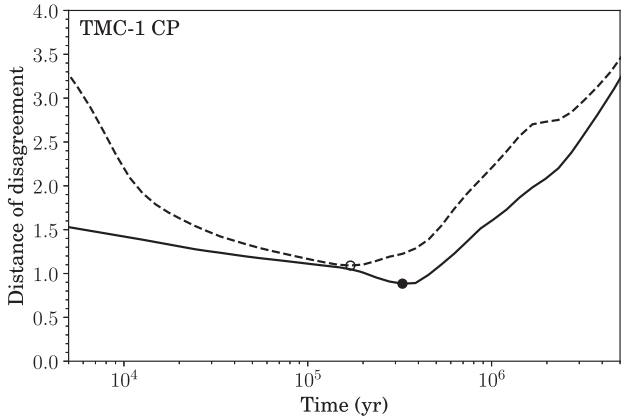

Figure 8. Distance of disagreement of molecules between TMC-1 CP and the model with low-metal initial abundances. Dotted and solid lines indicate models without and with PAHs, respectively. Points mark the best-fitting ages.

PAH chemistry, shock chemistry, high-temperature chemistry and physical conditions should also be considered carefully and self-consistently in outflows in future work.

3.3.2 Gas-phase molecules observed in TMC-1

Although Wakelam & Herbst (2008) have made a comparison between observations and models to TMC-1 using a pure gas-phase model with PAHs, we re-do this to show that introducing PAHs into a three-phase model does not change their conclusions. We also show the abundance values that will be useful to find disagreements between observations and models, especially for some S-bearing species. Thus, a possible solution is proposed in Section 4 using high-metal initial abundances.

To quantify the disagreement between models and observations in TMC-1 CP, we use the distance of disagreement (Wakelam, Herbst & Selsis 2006)

$$D(t) = \frac{1}{N_{\rm obs}} \sum_{i=1}^{N_{\rm obs}} |\log(X_{{\rm obs},i}) - \log(X_{{\rm mod},i})| \quad (2)$$

to obtain the best fit, using a collection of observed species abundances (with respect to $n_{\rm H}$) collected by Agúndez & Wakelam (2013), CH_3CHO (10^{-10}) and $HCOOCH_3$ (1.1×10^{-10}) from Soma et al. (2018), and NS^+ (2.4×10^{-12}) from Cernicharo et al. (2018). In total, the number of observed species is $N_{\rm obs} = 56$. In equation (2), $X_{{\rm obs},i}$ and $X_{{\rm mod},i}$ are abundances from observations and models, respectively. We show calculated $D(t)$ in Fig. 8, which shows that the model with PAHs produces a better overall agreement (smaller D value) with molecules in TMC-1 CP. The chemical ages are constrained as 3.3×10^5 and 1.7×10^5 yr for the model with and without PAHs, respectively. The comparison of gas-phase abundances between observations and models in TMC-1 CP is shown in Fig. 9. From this figure, we see that OCS, HC_5N, HC_7N, HC_9N, CH_3OCH_3, C_3H_4, C_3H_3N, CH_3C_6N and CH_3CHO have enhanced abundances by more than one order of magnitude (red vertical lines), reaching observed levels due to the inclusion of PAHs.

However, for CH_3OH and CH_3OCH_3, models with PAHs still underestimate their abundances. This could be due to the missing non-thermal desorption: reactive desorption (e.g. Garrod et al. 2007; Minissale et al. 2016) and/or grain size-dependent cosmic ray induced desorption (e.g. Iqbal & Wakelam 2018) in our model. If non-thermal desorption is properly treated together with PAHs, a better agreement is expected when feedback from dust grains makes reasonable contributions to gas-phase COMs. We note that

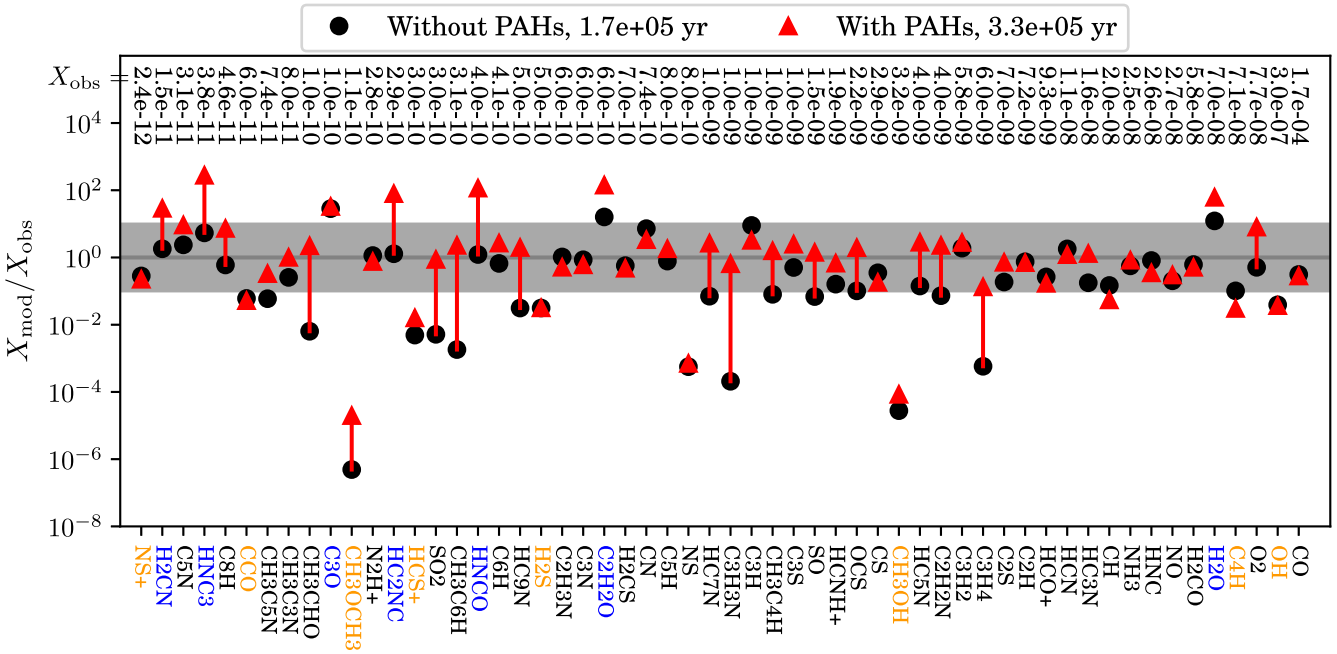

Figure 9. The ratios ($X_{\rm mod}/X_{\rm obs}$) of 56 gas-phase molecular abundances (X, with respect to $n_{\rm H}$) between models with low-metal initial abundances and observations in TMC-1 CP (Agúndez & Wakelam 2013; Cernicharo et al. 2018; Soma et al. 2018). Points and triangles are for models without and with PAHs, respectively. The light grey region shows one order of magnitude of assumed uncertainties of the observed value. The observed abundances are shown with labels at the top of this figure. The red lines mark differences by more than one order of magnitude between models. The chemical formulas with blue and orange colours indicate the species overestimated and underestimated by our model with PAHs, respectively.

Table 3. Abundance (relative to n_H) of neutral S-bearing species in the gas phase (left part), dust surface (middle part) and mantle (right part) from the model with high-metal initial abundance at the age of 2×10^6 yr. In each part, the first and second columns show abundances from models without (X) and with (X^{PAH}) PAHs, respectively. The third column shows the relative change of abundance, $RC = (X^{PAH} - X)/X$, caused by the inclusion of PAHs. Bold font indicates a negative change ($RC < 0.0$).

Species	Gas phase			Dust surface			Dust mantle		
	X	X^{PAH}	RC	X	X^{PAH}	RC	X	X^{PAH}	RC
H_2S	7.45e–10	3.78e–09	4.1	1.31e–06	1.38e–06	0.053	1.35e–05	1.30e–05	**−0.03**
SO	2.69e–09	1.22e–08	3.5	3.72e–11	2.56e–10	5.9	2.48e–12	3.33e–09	1.3e+03
SO_2	4.24e–11	4.37e–10	9.3	2.46e–18	1.87e–17	6.6	6.61e–14	2.06e–08	3.1e+05
OCS	1.89e–11	1.11e–10	4.9	1.19e–15	1.67e–15	0.4	9.77e–13	5.70e–08	5.8e+04
HCS	6.99e–11	1.94e–10	1.8	1.08e–19	3.45e–19	2.2	9.43e–20	1.08e–18	10
S_2	5.53e–11	8.46e–10	14	9.27e–10	6.92e–09	6.5	6.44e–14	3.34e–12	51
S	2.14e–07	2.32e–07	0.085	2.03e–15	2.34e–15	0.16	2.71e–13	6.04e–13	1.2
CS	8.33e–10	7.27e–10	**−0.13**	1.41e–10	1.61e–09	10	3.06e–13	3.25e–10	1.1e+03
C_2S	5.06e–11	1.48e–10	1.9	1.55e–12	1.71e–11	10	1.57e–15	4.04e–12	2.6e+03
C_3S	8.78e–12	5.58e–11	5.4	4.23e–09	1.36e–07	31	1.25e–11	1.54e–08	1.2e+03
C_4S	2.21e–13	2.93e–12	12	1.94e–11	1.74e–08	900	3.61e–16	2.83e–10	7.8e+05
H_2CS	3.03e–09	3.53e–09	0.16	1.02e–08	2.84e–08	1.8	3.29e–11	4.07e–10	11
HS	8.70e–11	1.16e–09	12	3.62e–15	4.52e–15	0.25	1.20e–12	9.49e–09	7.9e+03
NS	4.22e–10	6.62e–10	0.57	4.53e–14	1.18e–13	1.6	7.26e–14	1.30e–09	1.8e+04
HS_2	1.10e–11	3.02e–10	26	1.89e–10	1.80e–09	8.5	6.75e–15	3.71e–13	54
H_2S_2	1.06e–11	8.89e–10	83	1.83e–10	7.83e–09	42	6.41e–15	7.92e–12	1.2e+03
SIS	4.54e–13	5.80e–12	12	6.92e–10	1.19e–08	16	1.03e–13	2.97e–11	2.9e+02

abundances of some species are overestimated by our model with PAHs such as, H_2CN, HNC_3, HC_2NC, HNCO, C_2H_2O and H_2O (blue chemical formulas in Fig. 9). These disagreements will be mostly removed when both PAHs and high-metal abundances are considered (see Appendix C). We also note that our model with PAHs cannot reproduce S-bearing species abundances well, such as NS, H_2S and HCS^+ (orange chemical formulas in Fig. 9). We discuss these S-bearing species using a model with PAHs and high-metal initial abundances in Section 4.

4 EFFECTS OF PAHS ON S-BEARING SPECIES USING HIGH-METAL ABUNDANCES

The initial abundances play an important role in chemistry, especially for sulphur-bearing species that have two widely used initial abundances: a depleted value ($\sim 10^{-8}$) and the cosmic value ($\sim 10^{-5}$; e.g. Wakelam & Herbst 2008; Vidal et al. 2017; Laas & Caselli 2019). To compare the differences with the model using low-metal initial abundances, we tested the EA2 set with high-metal initial abundances from Wakelam & Herbst (2008); see the third column in Table 1. Compared with the low-metal initial abundances in the second column of Table 1, the metal abundances in high-metal set are enhanced by about two to three orders of magnitude, but the same for others. This allows us to explore the effects of initial abundances, especially for S-bearing species that are greatly affected by PAHs, as shown in the following.

We show all neutral S-bearing species from the model with high-metal initial abundances at 2×10^6 yr (see the determination of the age in Section 4.2) in Table 3. This table shows that the inclusion of PAHs introduces big changes to abundances of gas-phase (right part), dust surface (middle part) and mantle (right part) species. In each part, the third column shows the relative change of abundance $RC = (X^{PAH} - X)/X$, which can be easily used to check the effects of PAHs. In general, the inclusion of PAHs produces enhanced abundances for most S-bearing species, but reduced abundances of CS in the gas phase and H_2S in the mantle. In the following subsections, we discuss S-bearing species in the solid and gas phases by comparing them with observations.

4.1 Ice fractions

We show the ice fractions of selected species in Fig. 10. From this figure, we see that the high-metal initial abundances do not change the main composition (H_2O, CO, CO_2, NH_3 and PAHs) much. However, SO, SO_2 and OCS have big enhancements up to three orders of magnitude using the high-metal initial abundances. Their ice fractions are also consistent with the observed upper limits of OCS (0.2) towards Elais 16 (see collected data in Gibb et al. 2000) and SO_2 (0.6) towards W33A (Boogert et al. 1997). The inclusion of PAHs provides an alternative way to produce a comparable ice fraction of OCS, which cannot be reproduced well by most of the previous chemical models resulting in an OCS ice fraction of only $\sim 10^{-14}$–10^{-9} (e.g. Ruffle & Herbst 2000; Garrod et al. 2007; Acharyya, Hassel & Herbst 2011). This is also consistent with the recent modelled ice fraction of OCS using an enhanced reaction network and the cosmic value of sulphur at the age of a few 10^6 yr (Vidal et al. 2017; Laas & Caselli 2019). For COMs (CH_3OH, $HCOOCH_3$ and C_2H_5OH), the effects of initial abundances are small.

In our model with PAHs and high-metal initial abundances (see Table 3 and Fig. 2), 99 per cent of elementary sulphur is locked in solid-phase H_2S with an abundance of $X \sim 10^{-5}$ at the age of 2×10^{-6} yr. The OCS, SO, SO_2, C_3S, HS and NS are the secondary abundant S-bearing species in ice with abundances of $X \sim 10^{-9}$–10^{-8}. These are consistent with the modelled organo-sulphur in ice by Laas & Caselli (2019).

Here, we only present the leading reactions for the main S-bearing species (H_2S, SO, SO_2 and OCS) in ice. With high-metal abundance of S^+ and PAHs, the most abundant H_2S is formed in the dust surface via

$$H + HS \longrightarrow H_2S \ (\sim 100 \text{ per cent}), \quad (3)$$

without change compared with the model without PAHs. The H_2S is destroyed through $H_2S + H \longrightarrow HS + H_2$ in the solid phase, which

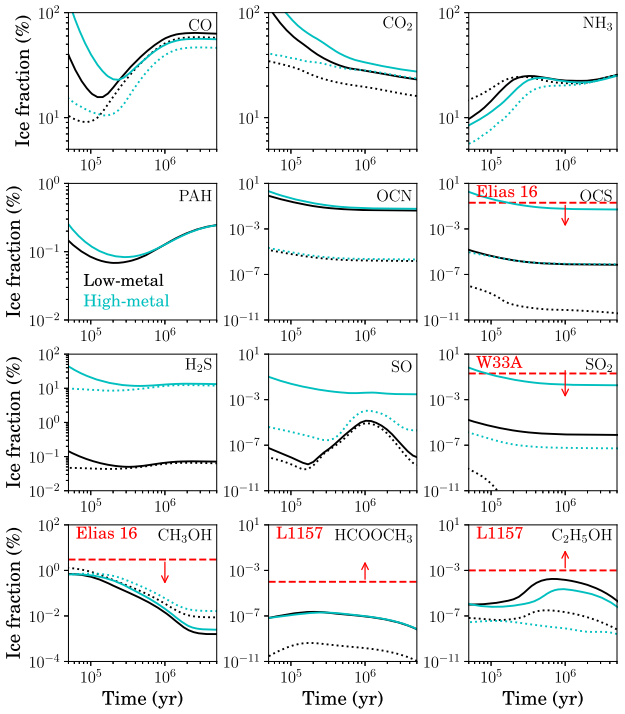

Figure 10. Ice fractions (in per cent, relative to water) from models using low-metal (black colour; see second column of Table 1) and high-metal (cyan colour; see third column Table 1) initial abundances. The dotted and solid lines are for models without and with PAHs, respectively. Horizontal lines indicate upper limits for OCS and CH_3OH in Elias 16 (see Table 2), SO_2 in W33A (Boogert et al. 1997) and lower limits for $HCOOCH_3$ and C_2H_5OH deduced from L1157 (see Table 2) roughly.

is the same as that in Vidal et al. (2017). The solid-phase OCS is formed through the following two reactions in the dust surface:

$$\mathrm{CO + S \longrightarrow OCS\ (\sim 95\ per\ cent);} \quad (4)$$

$$\mathrm{CS + O \longrightarrow OCS\ (\sim 5\ per\ cent).} \quad (5)$$

The enhancement of SO ice abundance (mantle + surface) is due to the direct accretion of enhanced gas-phase SO. However, for SO_2, it is mainly formed through enhanced reactions in ice,

$$\mathrm{SO + O \longrightarrow SO_2\ (\sim 100\ per\ cent),} \quad (6)$$

due to the enhanced abundance of ice SO.

If correlations of ice composition between protostar IRAS 16293–2422 B and comet 67P/Churyumov–Gerasimenko (67P/C–G) found by Drozdovskaya et al. (2019) are true, we can roughly compare the ice S-bearing abundance with that observed in comet 67P/C–G (Calmonte et al. 2016; Shingledecker et al. 2020). We list our modelled ice abundances of S-bearing species in Table 4 together with those observed, which shows that our model with PAHs (third column) produces a better agreement than the model without PAHs (second column). Additionally, our model with PAHs can reproduce PN, PO and HCl. In other words, the observed data in the comet prefer the model with PAHs.

4.2 Gas-phase sulphur-bearing abundances

By comparing 11 collected S-bearing species, Vidal et al. (2017) proposed a best chemical age of 1.3×10^6 yr for TMC-1 CP using an enhanced S-bearing network with high-metal initial abundances. We also checked the effects of initial abundances on gas-phase S-bearing species. We use the same function shown in equation (2) to calculate a distance of disagreement among 10 selected S-bearing species but without HNCS and HSCN, which are not in our network. However, we added a new observed species NS^+ (Cernicharo et al. 2018) to compare with our model.

The calculated $D(t)$ is shown in Fig. 11 using all ten species shown in Fig. 12. The best-fitting age of 2×10^6 yr for the model with high-metal initial abundances and PAHs is marked with a vertical yellow line in Fig. 11. This age is strongly supported by the total abundance of the detected gas-phase S-bearing abundance, $X_{\rm tot}^{\rm detected}(\mathrm{S})$ (red solid line); see Fig. 13. At the best age, the total abundance of all S-bearing species $X_{\rm tot}(\mathrm{S}) \sim 2.8 \times 10^{-7}$ is very close to the total abundance of the ten detected gas-phase species in TMC-1 (2.6×10^{-8}, red dash-dotted line) and the depleted sulphur abundance of 8×10^{-8} widely used in dark cloud models (black dotted line). We also note the difference of the total abundances between all and only-detected S-bearing species. This means that the missing sulphur by observations in the gas phase is mainly locked in atom S (see Table 3). Also, around

Table 4. Abundances (relative to solid-phase H_2O) of ice sulphur-bearing species, PN, PO and HCl, from the model with high-metal initial abundances at 2×10^6 yr and from observations toward comet 67P/C–G. The second and third columns show the results from models without and with PAHs, respectively.

Species	Model	Model + PAHs	Comet 67P/C–G
H_2S	1.24×10^{-1}	1.36×10^{-1}	$(1.10 \pm 0.05) \times 10^{-2}$ [a]
OCS	8.23×10^{-9}	5.37×10^{-4}	$(4.08 \pm 0.09) \times 10^{-4}$ [a]
SO	3.34×10^{-7}	3.38×10^{-5}	$(7.10 \pm 1.10) \times 10^{-4}$ [a]
SO_2	5.56×10^{-10}	1.94×10^{-4}	$(1.27 \pm 0.03) \times 10^{-5}$ [a]
S_2	3.90×10^{-6}	3.26×10^{-5}	$(1.97 \pm 0.35) \times 10^{-5}$ [a]
H_2CS	8.65×10^{-5}	2.72×10^{-4}	$(2.67 \pm 0.75) \times 10^{-6}$ [a]
H_2S_2	7.72×10^{-7}	3.69×10^{-5}	$< 6.04 \times 10^{-6}$ [b]
HS_2	7.96×10^{-7}	8.50×10^{-6}	$< 1.06 \times 10^{-6}$ [b]
PO	1.44×10^{-6}	4.49×10^{-5}	$\sim 1.10 \times 10^{-4}$ [b]
PN	2.07×10^{-5}	2.14×10^{-4}	$< 1.10 \times 10^{-5}$ [b]
HCl	7.78×10^{-6}	2.55×10^{-4}	$\sim 1.40 \times 10^{-4}$ [b]

[a] Data from Calmonte et al. (2016) and Shingledecker et al. (2020). [b] Data from Drozdovskaya et al. (2019), and references therein.

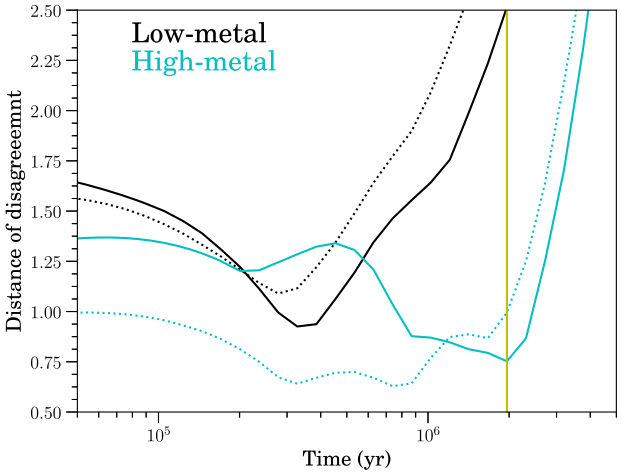

Figure 11. Distance of disagreement of ten S-bearing species from models with low-metal (black) and high-metal initial abundances (cyan). Solid and dotted lines indicate models with and without PAHs, respectively. The yellow vertical line marks the best-fitting age by the model with PAHs and high-metal initial abundances.

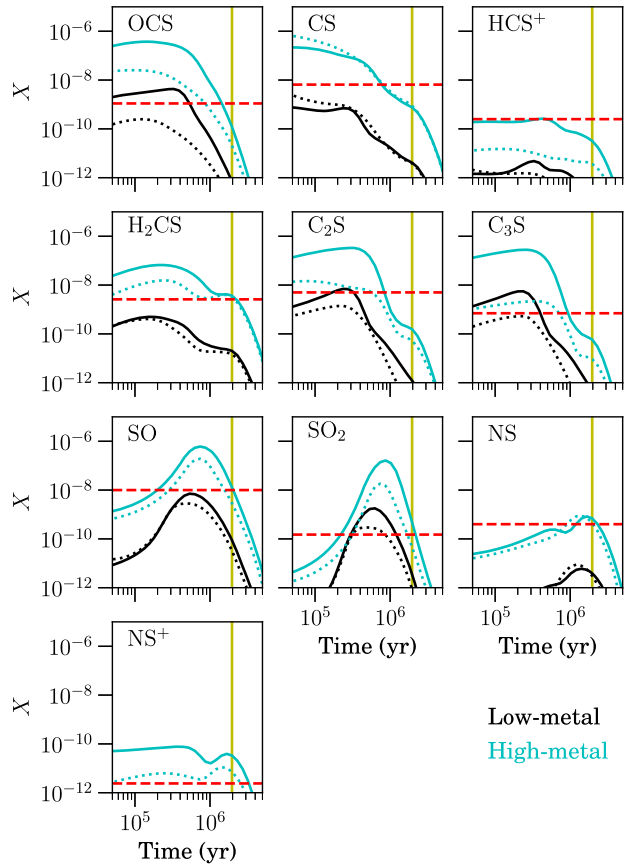

Figure 12. Gas-phase sulphur-bearing species abundance evolution tracks from three-phase models with low-metal (black) and high-metal (cyan) initial abundances. Solid and dotted lines indicate models with and without PAHs, respectively. The red dashed line marks the observed value in TMC-1 CP. The yellow vertical line marks the best-fitting age by the model with PAHs and high-metal initial abundances.

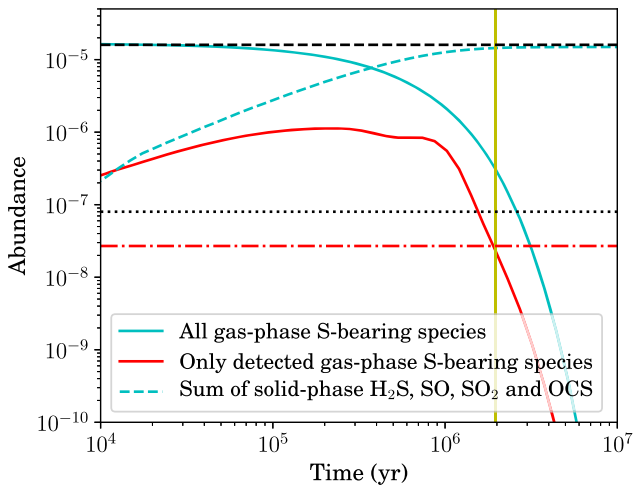

Figure 13. Total (selected) gas-phase and solid-phase S-bearing species abundances as a function of time (see legend). The yellow vertical line marks the best-fitting age by the model with PAHs and high-metal initial abundances. The dashed, dotted and dash-dotted horizontal lines denote initial high-metal S^+ abundance, low-metal S^+ abundance and total gas-phase abundance, respectively, of detected S-bearing species in TMC-1 CP.

10^6 yr (see Appendix C), other detected species can be reproduced by our model with PAHs and high-metal initial abundances.

From Fig. 11, we see that when no PAHs are included (dotted lines), our models reach best fits at the age of about $\sim 3 \times 10^5$ yr for models using low- and high-metal initial abundances. However, $D_{\rm min}$ is larger than in the model with high-metal initial abundances. Our model with high-metal initial abundances but without PAHs (cyan dotted line) produces two comparable good fits at $\sim 3 \times 10^5$ and $\sim 8 \times 10^5$ yr, respectively. However, HCS^+ abundance (Fig. 12) cannot be reproduced at any age of the two models. Our model with high-metal initial abundances and PAHs produce the best fit at $\sim 2 \times 10^6$ yr, which is consistent with that of Vidal et al. (2017) and Laas & Caselli (2019), using the cosmic value of the sulphur element and an enhanced reaction network for sulphur-bearing species. This all hints that combining PAHs into a gas–grain model provides an alternative way to produce observed gas-phase S-bearing species together with the ice OCS.

We also note that, at a wider age range of about $10^5 \sim 2 \times 10^6$, HCS^+ abundance can only be reproduced by the model with PAHs and high-metal initial abundances (cyan solid lines in Fig. 12). Meanwhile, our models can also reproduce the observed ratio ($\sim$33) between NS and NS^+ reported by Cernicharo et al. (2018) within a factor of 2, at the age of $\sim 2 \times 10^6$ yr.

In the model with PAHs and high-metal initial abundances, the formation pathway may be different from the model without PAHs. Because we used the PAH-related network of Wakelam & Herbst (2008), we re-describe the leading reactions for only HCS^+ and C_3S, which have bigger enhancements than others, to emphasize the importance of PAHs at the age of 2×10^6 yr. The abundance of HCS^+ is enhanced through

$$H_3O^+ + CS \longrightarrow HCS^+ + H_2O \quad (7)$$

$$CS^+ + H_2 \longrightarrow HCS^+ + H \quad (8)$$

$$H_3^+ + CS \longrightarrow HCS^+ + H_2 \quad (9)$$

in which H_3O^+ has enhanced abundance caused by PAHs (see Fig. B2).

For C_3S, the leading formation pathway is

$$HC_3S^+ + PAH^- \longrightarrow PAH + C_3S + H \quad (10)$$

together with the normal pathway

$$HC_3S^+ + e^- \longrightarrow C_3S + H. \quad (11)$$

All of the above leading reactions are mostly consistent with the ones from Laas & Caselli (2019) except for the PAH-related reactions. Considering the good agreements of all 11 gas-phase species in our model at the age of about $10^6 \sim 2 \times 10^6$ yr (see Fig. 12) and the good agreement of ice OCS, we emphasize the importance of PAHs in dark clouds, which is highly desired for studies in the future using experiments, models and observations.

5 EFFECTS OF THE SIZE AND ABUNDANCE OF PAHS

In our models, we have used the size (4 Å) and abundance (3.1×10^{-7}) of PAHs ($C_{30}H_{14}$) that produce the maximum effect on the chemical abundances in the pure gas-phase models from Wakelam & Herbst (2008). These parameters of PAHs are highly uncertain. In this section, we discuss the effects of the size and abundance of PAHs on S-bearing species. Wakelam & Herbst (2008)

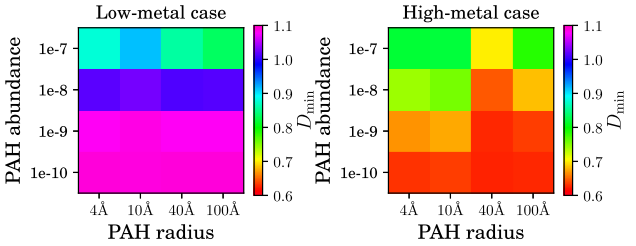

Figure 14. The calculated minimum distance of disagreement (D_{min}, colour scale) for models with varying radius and abundance of PAHs. The left and right panels are for low- and high-metal cases, respectively, with chemical ages of 2.0−2.5 × 10^5 and 0.8−2 × 10^6 yr accordingly.

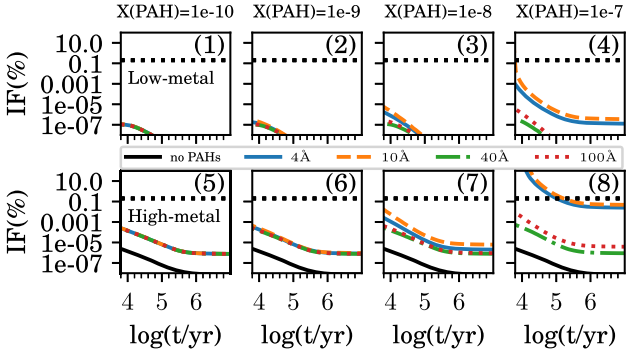

Figure 15. Ice fraction (IF, per cent) of OCS (surface + mantle) for models with varying PAH abundances (see text at the top: 10^{-10}, 10^{-9}, 10^{-8} and 10^{-7}) and radius (see legends between upper and lower panels: 4, 10, 40 and 100 Å). Upper and lower panels are for low- and high-metal cases, respectively. The black solid line indicates the model without PAHs. The black dotted line indicates the observed value.

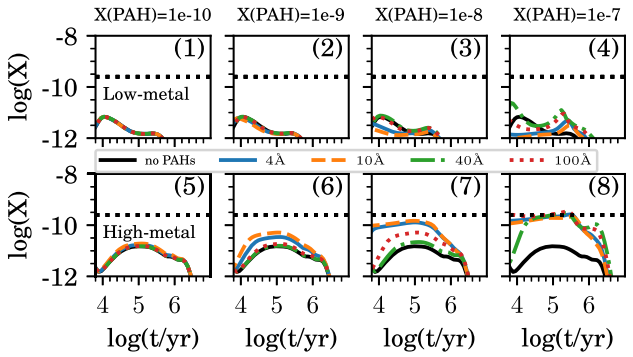

Figure 16. Similar to Fig. 15, but with the *y*-axis for HCS^+ abundance with respect to n_H. The black dotted line indicates the observed value.

have tested PAH abundance and radius in the ranges of 10^{-10}–10^{-7} and 4–400 Å, respectively, and found that high abundances of small PAHs are needed for the model with the EA2 set (high-metal set) to reproduce the observations in the cold core TMC-1. Thus, in this work, we test four typical PAH abundances of 10^{-10}, 10^{-9}, 10^{-8} and 10^{-7}, and four typical radii of 4, 10, 40 and 100 Å, which cover a smaller range of PAH radius than that in Wakelam & Herbst (2008). For the PAH radius-dependent recombinations rates between PAH^- and the position ion in the gas phase, we use their standard equation (4) with charge attraction for the model with a PAH radius of 4 Å. However, for models with radius ≥10 Å, we use their equation (6) without charge attraction. This is because several negative charges are more likely to neutralize larger PAHs and because the models of Wakelam & Herbst (2008) with a PAH radius larger 10 Å had shown bigger effects on the ionization fraction using equation (6) than using equation (4) (see their fig. 9). This is the biggest possible effect we want to check in this section. For these tests in this work, we used a fixed mass of PAH ($C_{30}H_{14}$), which means independence between PAH radius and mass, as adopted in Wakelam & Herbst (2008).

The above setting results in 16 (= 4 × 4) models for each set of the initial abundances: low- or high-metal set. In the following, we first calculate the distance of disagreement of the same ten S-bearing species adopted in Figs 11 and 12 to show the overall agreement. Then, two special species solid-phase OCS and gas-phase HCS^+ are discussed, which are sensitive to the inclusion of PAHs, as noted in Sections 4.1 and 4.2, respectively.

Fig. 14 shows the calculated minimum distance of disagreements (D_{min}, colour scale) of the 16 models for the low-metal (left panel) and high-metal (right panel) cases, respectively. The corresponding best chemical ages are overlaid on each cell with the logarithmic value. From this figure, for the low-metal case (left panel), we see that the best-fitting chemical ages are ∼2 × 10^5 yr at which the corresponding D_{min} are in the range of about 0.8–1.1 over all PAH radii and abundances. The better models are reached with a high PAH abundance of 10^{-7}. However, all PAH radii (4, 10, 40 and 100 Å) can be used to produce similar D_{min} at about 0.8–0.9, which makes it difficult to find the best model for the low-metal case. For the high-metal case (right panel), the best chemical ages are around 10^6 yr for all 16 models, at which all the values of D_{min} are in the range of about 0.6–0.8, which is better than that of the low-metal case. However, it is still difficult to constrain the parameter space of PAH by such a small range of D_{min} (0.2 corresponds to a factor of about $1.6 \approx 10^{0.2}$) for the high-metal case.

Thus, we try to constrain the parameter space of PAH by checking solid-phase OCS and gas-phase HCS^+. Fig. 15 shows the modelled ice fraction (per cent) of OCS and Fig. 16 shows the modelled abundance of HCS^+ with varied PAH abundance and radius in different panels. From the two figures, we see that the observed values (black dotted lines) of solid-phase OCS (Fig. 15) and gas-phase HCS^+ (Fig. 16) can only be reproduced by the models with high-metal initial abundance and high abundances of PAHs (see the bottom-right panels of the two figures) after ∼10^5 yr. For a general trend for solid-phase OCS (see panel 8 in Fig. 15), the model with a PAH radius of 100 Å is the intermediate case between the model with a PAH radius of 4 Å (solid blue line) and the model without PAHs (black solid line). This is the same trend for the ionization fraction (i.e. the sum of all positively or negatively charged species) in this work and in Wakelam & Herbst (2008).

To reproduce gas-phase HCS^+ (Fig. 16), the model with a PAH abundance of 10^{-8} prefers the PAH radii of 4 and 10 Å (see panel 7). However, for the model with PAH abundance of 10^{-7}, all PAH radii (4, 10, 40 and 100 Å; see panel 8) can be used to reproduce HCS^+ reasonably. This is because the balance between producing (e.g. via enhanced H_3O^+ + CS) and destroying (e.g. through e^-/PAH^- + HCS^+) reactions of HCS^+ in the gas phase is reached when the PAH abundance is high enough to simultaneously enhance H_3O^+ abundance. This is also true for other ions in the gas phase such as H_3O^+, HCS^+, OCS^+ and $HOCS^+$.

To reproduce solid-phase OCS, the PAH abundance of 10^{-7} and radii of 4 Å or 40 Å are needed (see panel 8 of Fig. 15). This is because the abundance of solid-phase OCS is affected by accretion and reactions (CO + S and CS + O) in the surface and/or mantle. The response of solid-phase OCS to PAH radii is similar to the response of solid-phase CS to PAH radii. When the PAHs are considered,

enhanced gas-phase CnS ($n = 1, 2, 3, 4$) via $PAH^- + HCnS^+$ ($n = 2, 3, 4$) is mainly transferred to the solid phase via accretion. Then, the solid-phase C_2S reacts with the C atom to form C_3S in the solid phase. However, C_3S cannot be efficiently transferred to C_4S as C_3S has bigger diffusion energy than C_2S, which results in slower diffusion. However, the solid-phase C_3S and C_4S can be destroyed to form CS, which is then transferred to OCS through CS + O in the solid phase. Thus, CS + O $\longrightarrow$ OCS also makes a contribution to the formation of OCS in the solid phase. Finally, we see that C_3S and OCS are the two most abundant in the solid phase except for H_2S, SO and SO_2 (see Table 3), and the solid-phase OCS has a large enhancement and positive response to the abundances of PAHs. However, it is unnecessary to trace/discuss more details because we have simply assumed independence between PAH radius and mass, which may introduce uncertainties.

For a summary, to reproduce OCS and HCS^+, a high abundance ($\geq 10^{-7}$) of small PAHs (≤ 10 Å) is necessary when high-metal initial abundances are used. This is consistent with the conclusions from Wakelam & Herbst (2008) for better reproducing the abundances of all the observed gas-phase species (see their fig. 11, panel 2-a). However, it should always be kept in mind that the chemical effects are strongly dependent on the sizes and abundances of PAHs, and this will require future experiments and observations to constrain the roles of PAHs.

6 SUMMARY

We have investigated the effects of PAHs on molecular abundances in dark clouds using a three-phase gas–grain chemical model with PAH-related chemistry. A good overall agreement in both the gas phase and ice hints at the importance of PAHs in dark clouds. The inclusion of PAHs in gas–grain chemistry changes ice chemistry through accretion and/or reactions in ice when gas-phase species have comparable/larger abundances than in the solid phase. Our main findings are as follows.

(i) At the typical ages of dark clouds ($\sim 10^5 - 10^6$), some simple (e.g. OCS and OCN) and complex organic molecules (e.g. C_2H_5OH and $HCOOCH_3$) in the solid phase have enhanced abundances by more than two orders of magnitude due to the inclusion of PAHs. The inclusion of PAHs introduced additional formation pathways for ice OCS via the dust surface in the model with low-metal initial abundances at 10^6 yr: CS + O $\longrightarrow$ OCS ($\sim$10 per cent) and accretion from gas-phase OCS ($\sim$10 per cent), together with the normal one: CO + S $\longrightarrow$ OCS ($\sim$80 per cent). For the model with PAHs and high-metal initial abundances, CS + O $\longrightarrow$ OCS and CO + S $\longrightarrow$ OCS make $\sim$5 and $\sim$95 per cent contributions, respectively.

(ii) Considering that carbon atoms in ice are mainly locked in CO and CO_2, the elemental carbon fraction of ice PAH is estimated as $\sim$4 per cent, which is comparable to the observations ($\sim 2-30$ per cent).

(iii) The combination of PAHs, gas–grain reaction network and high-metal initial abundance could be a solution for producing the abundances of S-bearing species in both the gas phase (e.g. HCS^+) and ices (e.g. OCS).

(iv) Compared with ice abundances in comet 67P/C–G, the model with PAHs results in better agreement with S-bearing species, PN, PO and HCl.

(v) Enhanced ice organic molecular abundances caused by the inclusion of PAHs roughly supports the sputtering of the dust mantle by high-velocity shock in L1157 from the point of view of the organic molecular abundance ratios.

The gas–grain dark cloud models with the inclusion of PAHs predict reasonable gas-phase and ice molecular abundances. A complete reaction network of PAHs is highly desired in future to study the formation pathway of PAHs and to predict more observable PAHs in dark clouds for future observations. Future observations are highly desired to constrain the size and abundance of PAHs, which have significant effects on dark cloud chemistry.

DATA AND CODE AVAILABILITY

The data and code used in this study will be made available by the corresponding authors upon request.

ACKNOWLEDGEMENTS

We would like to thank the anonymous referee for very useful comments. JXG would like to thank Dr Jinhua He for comments and discussions, and acknowledges support from FONDECYT grant 3170768. DM acknowledges support from CONICyT project Basal AFB-170002. NI gratefully acknowledges support from CONICyT International Networks for young researchers Grant REDI170243 and CONICyT/PCI/REDI170243 and /REDES190113. YP acknowledges support from the National Natural Science Foundation of China under grant No. 11947064.

REFERENCES

Acharyya K., Hassel G. E., Herbst E., 2011, ApJ, 732, 73
Agúndez M., Wakelam V., 2013, Chemical Reviews, 113, 8710
Allamandola L. J., Tielens A. G. G. M., Barker J. R., 1985, ApJ, 290, L25
Arce H. G., Santiago-García J., Jørgensen J. K., Tafalla M., Bachiller R., 2008, ApJ, 681, L21
Bachiller R., Pérez Gutiérrez M., 1997, ApJ, 487, L93
Bakes E. L. O., Tielens A. G. G. M., 1998, ApJ, 499, 258
Boogert A. C. A., Schutte W. A., Helmich F. P., Tielens A. G. G. M., Wooden D. H., 1997, A&A, 317, 929
Boogert A. C. A., Gerakines P. A., Whittet D. C. B., 2015, ARA&A, 53, 541
Calmonte U. et al., 2016, MNRAS, 462, S253
Carelli F., Grassi T., Gianturco F. A., 2013, A&A, 549, A103
Cernicharo J. et al., 2018, ApJ, 853, L22
Dartois E., D'Hendecourt L., 1997, A&A, 323, 534
Demarais N. J., Yang Z., Martinez O., Wehres N., Snow T. P., Bierbaum V. M., 2012, ApJ, 746, 32
Draine B. T. et al., 2007, ApJ, 663, 866
Drozdovskaya M. N., van Dishoeck E. F., Rubin M., Jørgensen J. K., Altwegg K., 2019, MNRAS, 490, 50
Fayolle E. C., Öberg K. I., Cuppen H. M., Visser R., Linnartz H., 2011, A&A, 529, A74
Garrod R. T., 2008, A&A, 491, 239
Garrod R. T., Wakelam V., Herbst E., 2007, A&A, 467, 1103
Ge J. X., He J. H., Yan H. R., 2016a, MNRAS, 455, 3570
Ge J. X., He J. H., Li A., 2016b, MNRAS, 460, L50
Ge J. X. et al., 2020, ApJ, 891, 36
Gibb E. L. et al., 2000, ApJ, 536, 347
Hasegawa T. I., Herbst E., Leung C. M., 1992, ApJS, 82, 167
Herbst E., van Dishoeck E. F., 2009, ARA&A, 47, 427
Iqbal W., Wakelam V., 2018, A&A, 615, A20
Kamp I., Thi W. F., Woitke P., Rab C., Bouma S., Ménard F., 2017, A&A, 607, A41
Laas J. C., Caselli P., 2019, A&A, 624, A108
Lefloch B., Ceccarelli C., Codella C., Favre C., Podio L., Vastel C., Viti S., Bachiller R., 2017, MNRAS, 469, L73
Lepp S., Dalgarno A., 1988, ApJ, 324, 553
McElroy D., Walsh C., Markwick A. J., Cordiner M. A., Smith K., Millar T. J., 2013, A&A, 550, A36

McGuire B. A., Burkhardt A. M., Kalenskii S., Shingledecker C. N., Remijan A. J., Herbst E., McCarthy M. C., 2018, Science, 359, 202
Majumdar L. et al., 2017, MNRAS, 466, 4470
Matar E., Bergeron H., Dulieu F., Chaabouni H., Accolla M., Lemaire J. L., 2010, J. Chem. Phys., 133, 104507
Millar T. J., 1992, MNRAS, 259, 35P
Minissale M., Dulieu F., Cazaux S., Hocuk S., 2016, A&A, 585, A24
Nummelin A., Whittet D. C. B., Gibb E. L., Gerakines P. A., Chiar J. E., 2001, ApJ, 558, 185
Parker D. S. N., Zhang F., Kim Y. S., Kaiser R. I., Landera A., Kislov V. V., Mebel A. M., Tielens A. G. G. M., 2012, Proc. National Academy of Science, 109, 53
Ruaud M., Wakelam V., Hersant F., 2016, MNRAS, 459, 3756
Ruffle D. P., Herbst E., 2000, MNRAS, 319, 837
Semenov D. et al., 2010, A&A, 522, A42
Shingledecker C. N., Lamberts T., Laas J. C., Vasyunin A., Herbst E., Kästner J., Caselli P., 2020, ApJ, 888, 52
Sipilä O., Caselli P., Redaelli E., Juvela M., Bizzocchi L., 2019, MNRAS, 487, 1269
Snell R. L. et al., 2000, ApJ, 539, L101
Soma T., Sakai N., Watanabe Y., Yamamoto S., 2018, ApJ, 854, 116
Tang M. et al., 2019, ApJ, 887, 243
Thomas A. M., Lucas M., Yang T., Kaiser R. I., Fuentes L., Belisario-Lara D., Mebel A. M., 2017, Chem. Phys. Chem., 18, 1971
Tielens A. G. G. M., 2008, ARA&A, 46, 289
Vasta M. et al., 2012, A&A, 537, A98
Vidal T. H. G., Loison J.-C., Jaziri A. Y., Ruaud M., Gratier P., Wakelam V., 2017, MNRAS, 469, 435
Wakelam V., Herbst E., 2008, ApJ, 680, 371
Wakelam V., Herbst E., Selsis F., 2006, A&A, 451, 551
Wakelam V. et al., 2012, ApJS, 199, 21
Watson W. D., 1976, Rev. Mod. Phys., 48, 513

APPENDIX A: ADDED AND REMOVED REACTIONS

To combine the PAH-related network used by Wakelam & Herbst (2008) with our gas–grain network taken from Semenov et al. (2010) (both can be found in the kinetic astrochemistry data base[3]), we have added/removed some reactions. For producing reasonable gas-phase abundance of HNCO, we added 13 gas-phase reactions taken from the UMIST data base for astrochemistry[4] (McElroy et al. 2013), which were missed by the original reaction network. These reactions enhance HNCO abundance from $\sim 10^{-18}$ to a comparable level of $\sim 10^{-10}$. We removed three reactions of $H_2COHOCH_2^+$, which is a duplicate of $H_5C_2O_2^+$ in the original gas–grain reaction network. This modification results in comparable gas-phase abundance of CH_3OH to that of Wakelam & Herbst (2008); see Figs B1 and B2. We also removed ten PAH-related reactions because the F-bearing species, HC_4N^+, $SiC_2H_3^+$, SiC_4H^+, $H_3C_3^+$ and $H_2C_3^+$, are not in our network. All the above-mentioned reactions are listed in Table A1.

Table A1. Added and removed reactions.

Reaction	Note
HNCO-related gas-phase reactions	
$CH_2 + NO \longrightarrow HNCO + H$	Added
$H_2NCO^+ + e^- \longrightarrow HNCO + H$	Added
$H_2NCO^+ + e^- \longrightarrow NH_2 + CO$	Added
$H_3^+ + HNCO \longrightarrow H_2NCO^+ + H_2$	Added
$HNCO^+ + H_2 \longrightarrow H_2NCO^+ + H$	Added
$HNCOH^+ + e^- \longrightarrow HNCO + H$	Added
$HNCOH^+ + e^- \longrightarrow NH + HCO$	Added
$H_3^+ + HNCO \longrightarrow HNCOH^+ + H_2$	Added
$HNCO^+ + H_2 \longrightarrow HNCOH^+ + H$	Added
$He^+ + HNCO \longrightarrow HNCO^+ + He$	Added
$NCO^+ + H_2 \longrightarrow HNCO^+ + H$	Added
$OCN + H_3^+ \longrightarrow HNCO^+ + H_2$	Added
$HNCO^+ + e^- \longrightarrow OCN + H$	Added
Gas-phase reactions of $H_2COHOCH_2^+$	
$H3CO^+ + H_2CO \longrightarrow H_2COHOCH_2^+$	Removed
$H_2COHOCH_2^+ + e^- \longrightarrow CH_3OH + HCO$	Removed
$H_2COHOCH_2^+ + e^- \longrightarrow HCOOCH_3 + HCO$	Removed
PAH-related reactions	
$F^+ + PAH^- \longrightarrow PAH + F$	Removed
$HF^+ + PAH^- \longrightarrow PAH + HF$	Removed
$HF^+ + PAH^- \longrightarrow PAH + H + F$	Removed
$H_2F^+ + PAH^- \longrightarrow PAH + HF + H$	Removed
$HC_4N^+ + PAH^- \longrightarrow PAH + HC_4N$	Removed
$SiC_2H_3^+ + PAH^- \longrightarrow PAH + SiC_2H_3$	Removed
$SiC_4H^+ + PAH^- \longrightarrow PAH + SiC_4H$	Removed
$H_3C_3^+ + PAH^- \longrightarrow PAH + H_2C_3 + H$	Removed
$H_2C_3 + +PAH^- \longrightarrow PAH + H_2C_3$	Removed
$H_2C_3^+ + PAH^- \longrightarrow PAH + HC_3 + H$	Removed

APPENDIX B: COMPARISON OF GAS-PHASE ABUNDANCES BETWEEN THE THREE-PHASE MODEL AND PURE GAS-PHASE MODEL

In this section, we compare the abundances of selected gas-phase species from three-phase models and pure gas-phase models with low- and high-metal initial abundances, as listed in the left and right columns of Table 1, respectively, with and without PAHs. To do this, we reduced our three-phase reaction network (hereafter this model is called M3) to a pure-gas phase reaction network (hereafter called M1). As a comparison, a pure gas-phase reaction network, the same as in Wakelam & Herbst (2008), was re-established according to their description of their reaction network (hereafter called W1). Thus, the chemical effects of dust grains on gas-phase abundances can be checked.

We show selected species from figs 3–7 of Wakelam & Herbst (2008) in Figs B1 and B2 for the models with low- and high-metal initial abundances, respectively. The solid and dotted lines indicate the results from the models with and without PAHs, respectively. The yellow and red colours indicate the pure gas-phase and three-phase models, respectively. Modelled results from the model with PAHs of Wakelam & Herbst (2008) are shown with black crosses. From Figs B1 and B2, we can see the following.

(i) By comparing abundances in pure gas-phase models M1 (solid yellow line) with W1 (black crosses) of Wakelam & Herbst (2008), we see that the two models produce very similar abundance evolution tracks to most of the selected species. We note that our model M3 still underestimated the CH_3OH abundance by a factor of about 10, which requires effective non-thermal desorption mechanisms to

[3] kida.obs.u-bordeaux1.fr/networks.html
[4] http://udfa.ajmarkwick.net/

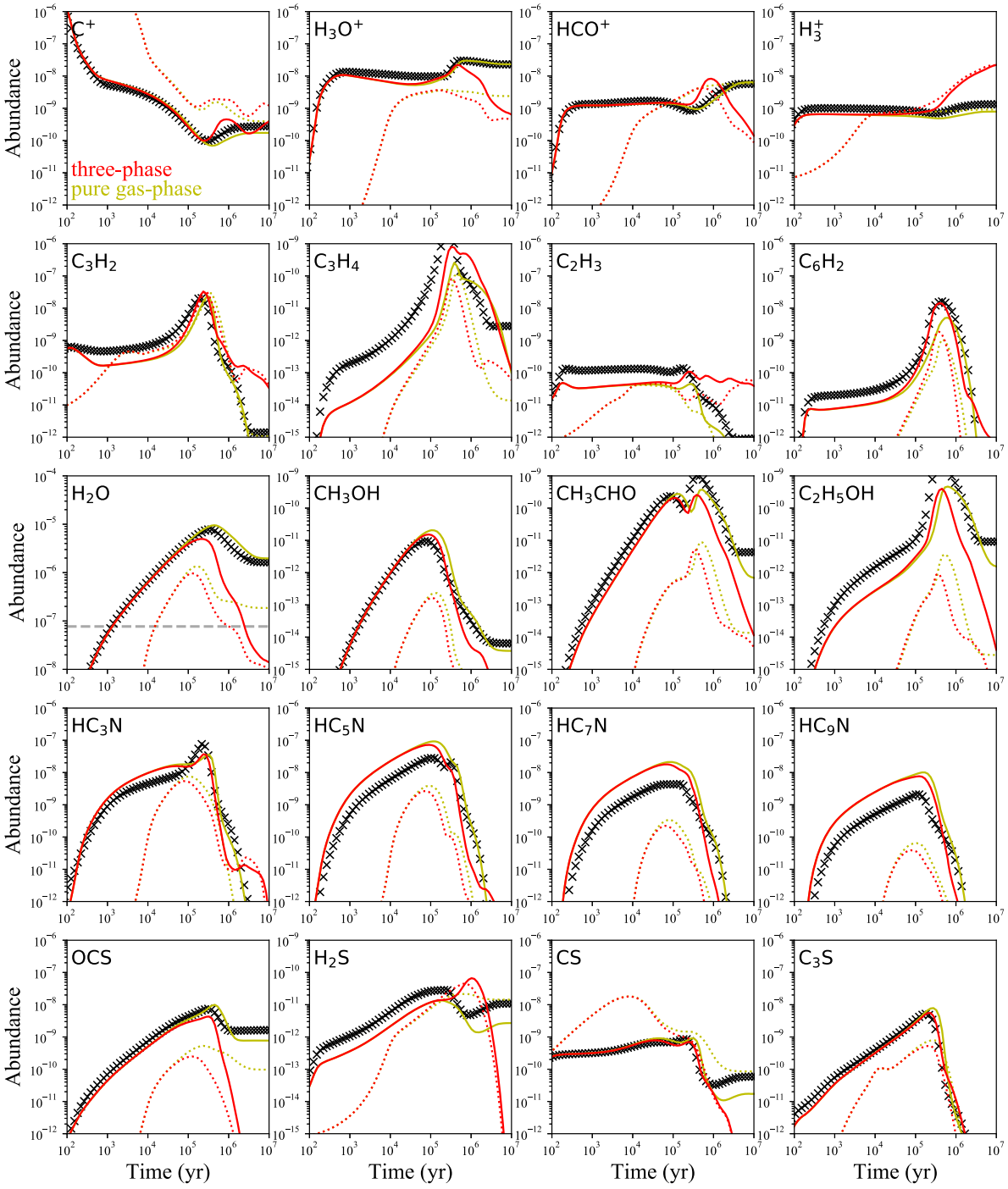

Figure B1. Abundances of selected gas-phase species from three-phase models (red lines) and pure gas-phase models (yellow lines) with low-metal initial abundances. Solid and dotted lines indicate the model with and without PAHs, respectively. Modelled results from the model with PAHs of Wakelam & Herbst (2008) are shown with black crosses as a comparison. The observed upper limit of H_2O is shown with a grey dashed line (Snell et al. 2000).

release CH_3OH from ice on dust grains, such as reactive desorption (Garrod et al. 2007; Minissale et al. 2016).

(ii) By comparing the pure gas-phase model M1 with the three-phase model M3, we see that the changes caused by changing the phase of the model are very small for most gas-phase species. However, for some species such as H_3O^+, H_3^+, H_2O, OCS and CS, the three-phase model produces earlier depletion, due to accretion.

In summary, changing the phase of the model does not alter the main conclusions about the effects of PAHs on gas-phase abundances from Wakelam & Herbst (2008).

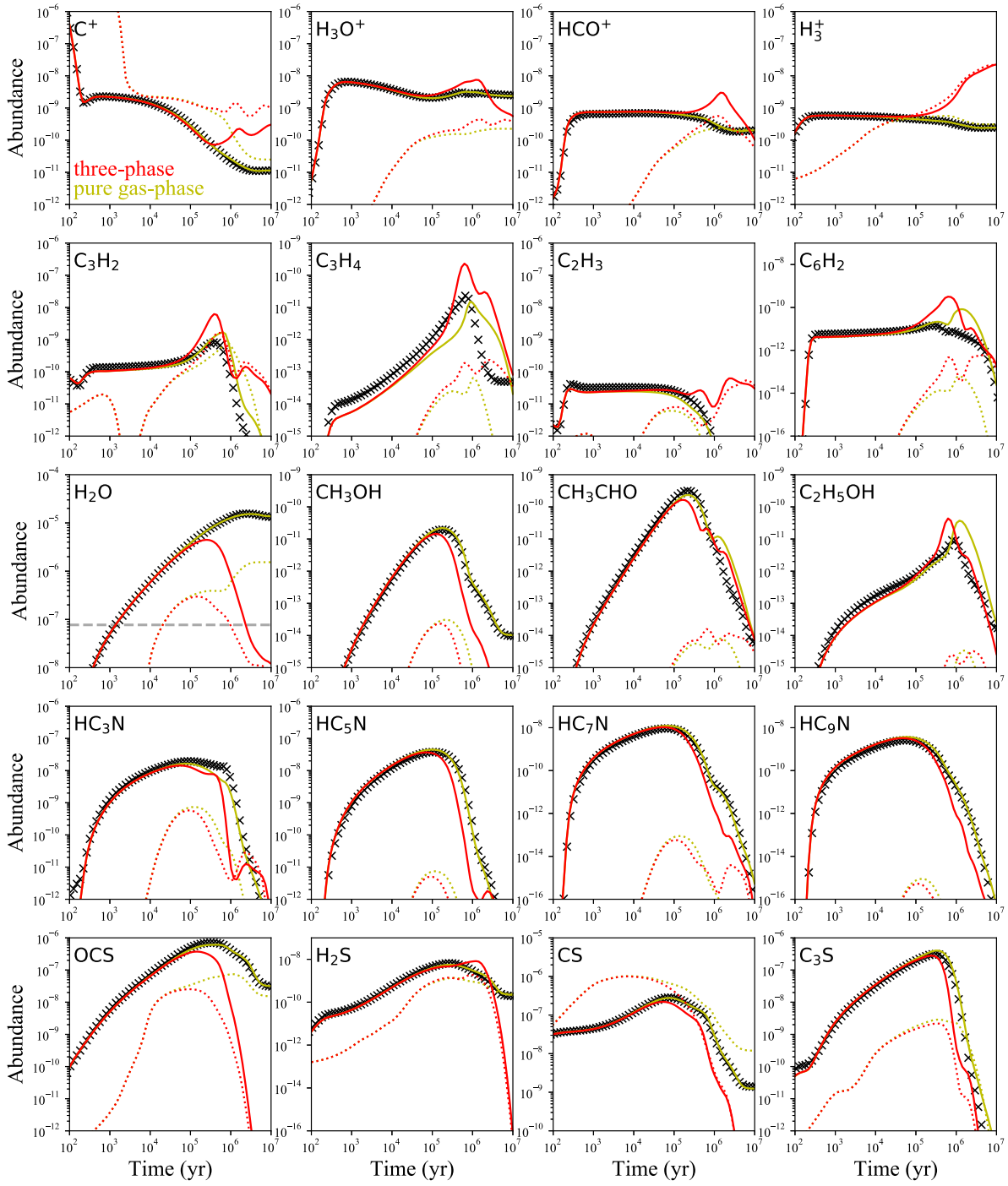

Figure B2. Same as Fig. B1 but for the model with high-metal initial abundances.

APPENDIX C: ABUNDANCE EVOLUTION TRACKS OF ALL DETECTED GAS-PHASE SPECIES

To show that our model with PAHs and high-metal initial abundances reaches good agreement for most of the detected gas-phase species in TMC-1 CP around 10^6 yr, we show our modelled abundance evolution tracks of 56 species in Fig. C1. From this figure, we see that most of the observed species can be reproduced at an age range of 5×10^5 to 2×10^6 yr, rather than the determined age of $\sim 10^6 - (2 \times 10^6)$ for only S-bearing species in Section 4.2. The large age range hints that the physical model and/or chemical network should be updated in a more self-consistent way to reach a better agreement at a single chemical age. This needs more efforts from both theoretical and experimental studies.

Compared with abundances from the model with PAHs and low-metal initial abundances shown in Fig. 9 (at the age of 3.3×10^5 yr), the model with PAHs and high-metal initial abundances produces better agreements for H_2O, HNCO, C_2H_2O, HC_2NC C_3O and C_5N around 10^6 yr. However, our models cannot reproduce the abundances of CH_3OH and CH_3OCH_3, which may be because of the missing non-thermal desorption processes (Garrod et al. 2007; Minissale et al. 2016; Iqbal & Wakelam 2018).

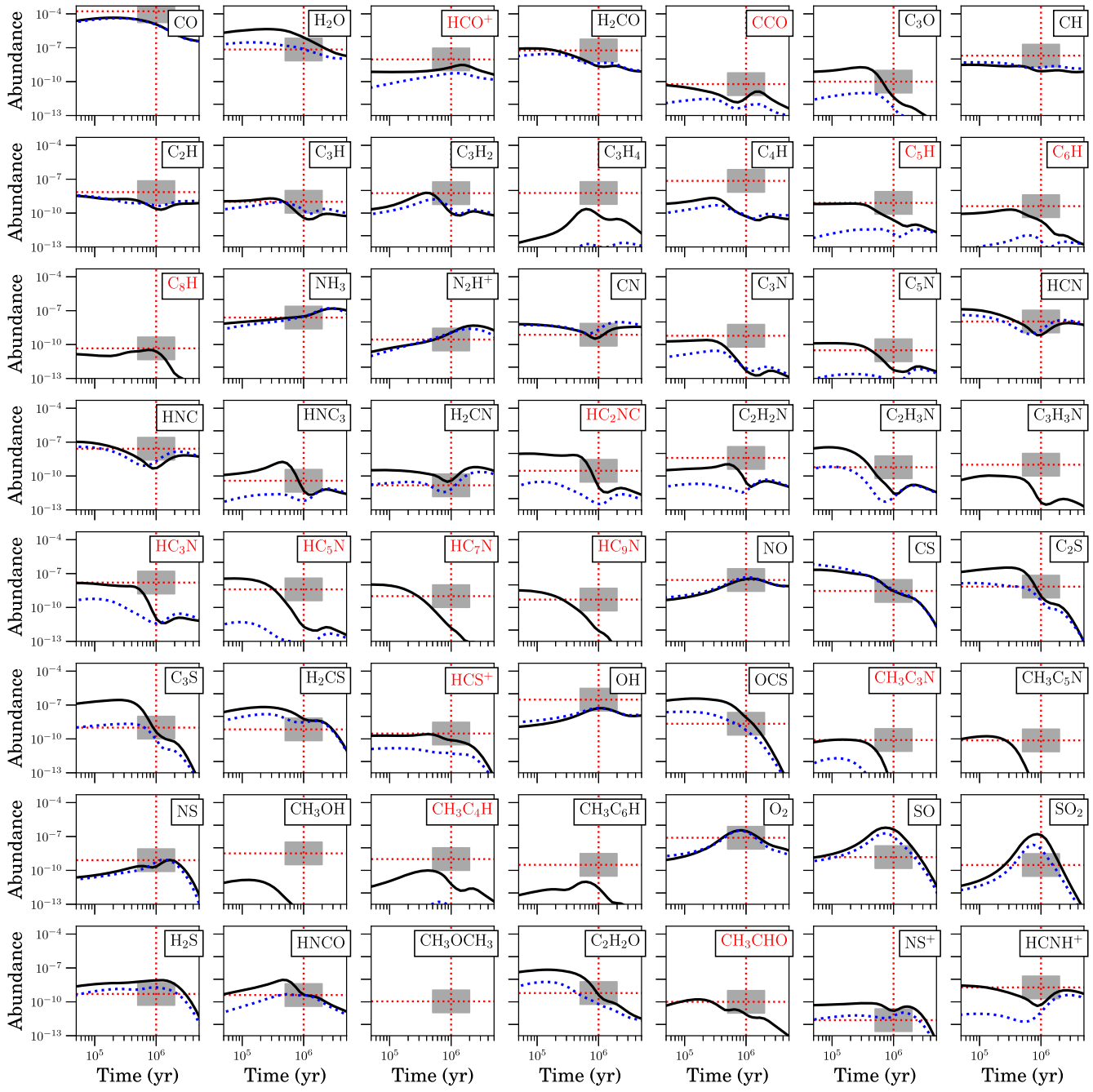

Figure C1. Abundance evolution tracks of 56 gas-phase species detected in TMC-1 from the model with high-metal initial abundances. The black solid and blue dotted lines show the models with and without PAHs, respectively. The grey region is jointly determined by the possible chemical age (5×10^5 to 2×10^6 yr with an age of 10^6 marked by a vertical red line) and the observed abundance (red horizontal line) with an uncertainty of one order of magnitude. Species with enhancements of agreement due to inclusion of PAHs are highlighted in red.

This paper has been typeset from a TEX/LATEX file prepared by the author.